The Cryosphere Discuss., 7, 4101–4176, 2013
www.the-cryosphere-discuss.net/7/4101/2013/
doi:10.5194/tcd-7-4101-2013

The Cryosphere Discussions
Open Access

Observing Muostakh Island disappear: erosion of a ground-ice-rich coast in response to summer warming and sea ice reduction on the East Siberian shelf

F. Günther[1], P. P. Overduin[1], A. Baranskaya[2], T. Opel[1], and M. N. Grigoriev[3]

[1]Alfred Wegener Institute Helmholtz Centre for Polar and Marine Research, Potsdam, Germany
[2]Lab. Geoecology of the North, Moscow State University, Moscow, Russia
[3]Melnikov Permafrost Institute, Russian Academy of Sciences, Siberian Branch, Yakutsk, Russia

Received: 28 June 2013 – Accepted: 29 July 2013 – Published: 15 August 2013

Correspondence to: F. Günther (frank.guenther@awi.de)

Published by Copernicus Publications on behalf of the European Geosciences Union.

Abstract

Observations of coastline retreat using contemporary very high resolution satellite and historical aerial imagery were compared to measurements of open water fractions and summer air temperatures. We analyzed seasonal and interannual variations of thawing-induced cliff top retreat (thermo-denudation) and marine abrasion (thermo-abrasion) on Muostakh Island in the southern central Laptev Sea. The island is composed of ground-ice-rich permafrost deposits of Ice Complex type that render it particularly susceptible to erosion along the coast, resulting in land loss. Based on topographic reference measurements during field campaigns, we generated digital elevation models using stereophotogrammetry, in order to block adjust and ortho-rectify aerial photographies from 1951 and GeoEye, QuickBird, WorldView-1, and WorldView-2 imagery from 2010 to 2012 for change detection. Coastline retreat for erosive segments ranged from −13 to −585 m and was -109 ± 81 m ($-1.8 \pm 1.3\,\mathrm{m\,a^{-1}}$) on average during the historical period. Current seasonal dynamics of cliff top retreat revealed rapid thermo-denudation rates of $-10.2 \pm 4.5\,\mathrm{m\,a^{-1}}$ in mid summer and $-4.1 \pm 2.0\,\mathrm{m\,a^{-1}}$ on average during the 2010–2012 observation period. Using sea ice concentration data from the Special Sensor Microwave Imager (SSM/I) and air temperature time series from Tiksi, we calculated seasonal duration available for thermo-abrasion, expressed as open water days, and for thermo-denudation, based on thawing degree days. Geomorphometric analysis revealed that total ground ice content on Muostakh is made up of equal amounts of intrasedimentary and macro ground ice, while its vertical hourglass distribution provides favorable local preconditions for subsidence and the acceleration of coastal thermo-erosion under intensifying environmental forcings. Our results showed a close relationship between mean summer air temperature and coastal thermo-erosion rates, in agreement with observations made for various permafrost coastlines different from East Siberian Ice Complex coasts elsewhere in the Arctic. Seasonality and recent interannual variations of coastline retreat rates suggest that the combination of macro

TCD
7, 4101–4176, 2013

ground ice distribution in the ground and changes in enviromental forcing generate a cyclicity in coastal thermo-erosion, that is currently increasing in frequency.

1 Introduction

Muostakh Island in Buor Khaya Gulf of the Laptev Sea is a small portion and a prominent example of thousands of kilometers of unstable coastline along marginal arctic shelf seas of East Siberia (Are, 1988a, b; Romanovskii et al., 2000; Grigoriev et al., 2009). Along this coast, ice-rich cliffs border marshy coastal tundra lowlands and islands that are underlain by continuous permafrost and composed of continental Late Pleistocene ice-rich permafrost sequences called Ice Complex deposits (Schirrmeister et al., 2013). During summer in the Laptev Sea region, this coast is no longer protected by sea ice (Eicken et al., 2005), and retreats at erosion rates of -2 to $-6\,\mathrm{m\,a^{-1}}$ (Grigoriev et al., 2006). On a long-term scale this corresponds to large areas of annual land loss of up to $-3400\,\mathrm{m^2}$ per kilometer of coastline and currently this process is more than twice as rapid as historical erosion (Günther et al., 2013). Given the short duration of the sea ice free period, erosional processes in the arctic coastal zone are very intense, due to the susceptibility of outcrops of unconsolidated deposits along non-rocky coasts to weathering. The distinguishing feature of polar coasts is the presence of a variety of ice types on and ground ice below the earth surface (Forbes and Hansom, 2011). Ogorodov (2011) emphasizes the influence of hydrometeorological conditions on the development of coastal thermo-erosion, in particular of thermal and wave energies, both of which are linked to sea ice extent and duration. For the Laptev Sea, Markus et al. (2009) report that the duration of the sea ice free season increased on average by 10 days over the last decade, exceeding the average increase of 2 days around the Arctic Ocean. This is explained by the time needed to lose additional heat gained during recently warmer summers (Steele et al., 2008). The higher heat content of surface waters in the Laptev Sea is partly the result of increasing water contributions from the Lena River (Bauch et al., 2013), whose discharge has significantly exceeded

TCD
7, 4101–4176, 2013

the historical average (Charkin et al., 2011). Especially when considering the warming trend of cold continuous permafrost (Romanovsky et al., 2010) and the vulnerability of deep organic carbon to mobilization (Grigoriev et al., 2004; Grosse et al., 2011), it is important to assess the impact of currently observed seasonal environmental changes in the Arctic as external forces on the erosion of ice-bonded permafrost coasts.

As a consequence of coastal erosion, clastic material enters the near shore zone (Are, 1998; Jorgenson and Brown, 2005), where it is deposited, reworked and transported (Overduin et al., 2007; Winterfeld et al., 2011). Because ground ice occupies a large proportion of the land's volume above and below sea level, a much smaller amount of material has to be removed by wave action after thaw when compared to ice-free coastlines and high rates of coastline retreat are the result (Zhigarev, 1998). Are et al. (2008) highlight the effect of ground ice content and grain size properties on thermo-erosion of ice-rich permafrost coasts, where thawing prevails over hydromechanical processes. They conclude that it is mostly thawed material that is being eroded, rather than permafrost. Because the silt fraction dominates, eroded material is easily transported far offshore.

Therefore, unlike thawing as a result of fluvial thermo-erosion, where running water is canalized along ice wedge polygon systems, or along river banks, coastal thermo-erosion includes two related processes that work temporally and quantitatively differently together. Thermo-denudation (TD) is comprised of the thawing of exposed permafrost, the upslope or inland propagation of a retreating headwall and the transport of material downward to the bottom, all under the influence of insolation and heat flux on the slope (Mudrov, 2007). Thermo-abrasion (TA), on the other hand, is defined as the combined action of mechanical and thermal energy of sea water at water level (Are, 1988a). Despite temporal variations in their intensity, both processes are interconnected, since thermo-denudation sooner or later becomes inactive after thermo-abrasion comes to a standstill.

Multitemporal applications of remote sensing data are of particular interest for assessing permafrost related hazards such as erosion of frozen sea coasts (Kääb, 2008).

TCD
7, 4101–4176, 2013

Arctic coastline recession rates are highly variable both spatially and temporally, and waves and storms are commonly accepted as a large, if not the largest, explanatory factor for arctic coastal erosion (Lantuit et al., 2011b). Numerous change detection studies in different permafrost settings throughout the Arctic exist and aimed to identify these arctic coastline variations by analyzing geodata time series in connection with other records. In concert with time lapse photography, Jones et al. (2009a) analyze the coastal erosion development around Cape Halkett using high resolution remote sensing data of the northern Alaska sea coast. They find that, after increasing slightly over the last five decades, annual erosion accelerated abruptly and almost doubled, reaching $-13.8\,\mathrm{m\,a^{-1}}$ from 2007 to 2009. They attribute this increase to more frequent block failure as a consequence of higher sea surface temperatures and longer fetch, which potentially create more erosionally effective storm events (Jones et al., 2009b). Lantuit et al. (2011a) study storm climatology and use a set of aerial photographs and satellite images to investigate erosion rates around the entire Bykovsky Peninsula near Tiksi in the Laptev Sea over five consecutive time periods. They show a clear dependency of coastal erosion on backshore thermokarst geomorphology, but do not find either a pronounced temporal trend in the mean annual coastal retreat rate ($-0.59\,\mathrm{m\,a^{-1}}$), nor a relation to storm activity, despite the long temporal coverage of 55 yr. For the western coast of the Yamal Peninsula, where retreat rates range from -0.8 to $-2\,\mathrm{m\,a^{-1}}$, Vasiliev et al. (2006) rely on long-term observational data of the polar station Marre Sale, where the length of the warm period is 102 – 137 days long, while the open water season lasts for 70 days on average, generating different preconditions for TD and TA. Although the Kara Sea region experiences frequent storms of long duration (Atkinson, 2005), Vasiliev et al. (2006) find that wave energy attributable to storms is less than 10 % of the total and that only in occasional cases up to 20 % of coastal retreat can be attributed to storms (Vasiliev, 2003). Arp et al. (2010) report on recent erosion for the Alaskan Beaufort Sea coast, where they observe even more rapid rates of up to $-17.1\,\mathrm{m\,a^{-1}}$, but find little correlation to sea surface and soil temperatures, and in particular no consistency with storm events. Although potential local controls on erosion

TCD
7, 4101–4176, 2013

such as ground ice content have been identified (e.g., Dallimore et al., 1996; Vasiliev, 2003), it is difficult to establish a relationship of erosion of permafrost coasts to one or another external factor. Moreover, since current changes in environmental parameters are expected to intensify coastal erosion, there is a sustained need for information on long-term and short-term coastline recession rates in conjunction with high resolution seasonal observations from different coastal settings in order to better understand the mechanisms driving thermo-erosion and subsequent land loss along permafrost–affected coasts.

The main objective of this paper is to systematically analyze seasonal thermo-erosion dynamics for a ground-ice-rich permafrost coast in the central Laptev Sea. We use a set of contemporary very high resolution satellite imagery, repeated geodetic surveys in the field and historical aerial photographs to provide current and historical quantifications of planimetric land loss and volumetric coastal erosion. In conjunction with digital elevation models, we use a geomorphometric method for assessing macro ground ice content of Ice Complex deposits, in order to consider this factor for the estimation of the mass of material that must be reworked by coastal thermo-erosion following thaw and the resulting sediment supply to the nearshore zone. Using time series of local sea ice concentration and air temperatures, we apply normalization to coastal retreat observations over seasonal and interannual periods to identify their seasonal intensity and to discuss environmental controls on processes involved in coastal thermo-erosion development.

2 Study Site

Muostakh is a small island (70° 35′ N 130° E), in the Buor Khaya Gulf of the southern central Laptev Sea (Fig. 1), located 40 km east of the harbour town Tiksi in northern Yakutia (Russian Federation). Though situated on the ocean, the severe subpolar climate with mean annual air temperatures in Tiksi of −11.5 °C, where the warmest month does not exceed 10 °C, is continental due to prolonged sea-ice cover. Muostakh

TCD
7, 4101–4176, 2013

lies within the northern tundra zone. The vegetation cover is characterized by moss-grass, lichens and dwarf shrub tundra. Cryogenic micro relief features are widespread and include mud boils, frost cracks, peat mounds, short steep thermo-erosional gullies, high-centred polygons on inclined surfaces and thermokarst mounds (baydzharakhs) on coastal bluffs. The island has an elongated narrow form oriented stretching SSE–NNW, approximately 7.5 km in length with a maximum width of ≤ 500 m at sea level. At the southern margin, next to the former polar station "Muostakh, Ostrov", a lighthouse marks the navigable channel into the sheltered Tiksi Bay. As a continuation of the island, an interrupted sand spit chain extends another 5.2 km southwards.

Grigoriev (1993) supposed that Muostakh Island was formerly connected with the Bykovsky Peninsula further in the north (Grosse et al., 2007), but nowadays they are separated by a distance of 15.8 km. Both, Bykovsky and Muostakh consist of Ice Complex deposits and their sedimentological and cryolithological structure suggests simultaneous formation (Slagoda, 2004). According to the Mamontovy Khayata section on Bykovsky, Ice Complex in this area formed from 58.4 to about 12.2 ka BP (Schirrmeister et al., 2002), and accumulated during the subaerial exposure of the East Siberian shelf, until they began to degrade by thermokarst processes at 13 – 12.4 ka BP (Romanovskii et al., 2000). Peat and wood on the base of the Holocene cover on Muostakh showed ages in the range of 2 to 7 ka BP. Muostakh represents a remnant of the Late Pleistocene accumulation plain that remained after the sea level drew to near the current level 8 ka ago (Gavrilov et al., 2006), and the highstand of the Holocene transgression was reached 5 cal. ka (Bauch et al., 2001). It serves as a witness for the widespread occurrence of Ice Complex islands on the shelf that have been completely destroyed by coastal thermo-erosion (Gavrilov et al., 2003). Ice-poor sands of Pliocene–Early Pleistocene age underlay Ice Complex deposits (Slagoda, 2004). Ice Complex thickness on Muostakh is 31 m, 10 m of which extend below sea level (Kunitsky, 1989; Grigoriev, 1993), providing very favourable conditions for thermo-abrasion.

According to Kunitsky (1989) the permafrost temperature of the non-degraded yedoma on Muostakh at the depth of zero amplitude is –10.4 °C, which is very cold per-

TCD
7, 4101–4176, 2013

mafrost and a typical value for Ice Complex uplands at this latitude in Northern Yakutia (Romanovsky et al., 2010). Since the Ice Complex was deposited in harsh Late Pleistocene climates under permafrost temperatures of −25 to −28 °C (Konishchev, 2002), it has already undergone considerable thermal degradation. Along 600 m on the west coast of Muostakh, a semi-circular fragment of a thermokarst depression (alas) is preserved, where Kunitsky (1989) reports an increase in temperature from −9.4 to −6 °C along a transect from the Ice Complex top down to the alas bottom close to the coast. However, according to Romanovsky et al. (2010), alas temperatures at this latitude are around −9 °C, illustrating that permafrost in the coastal zone of Muostakh has also undergone thermal degradation. Also in the south of the island around the polar station, Romanovskii et al. (2000) and Slagoda (2004) identfied fragments of an alas.

Regular stationary monitoring of coastal retreat in the Laptev Sea region is conducted only in two places: Mamontovy Khayata on the Bykovsky Peninsula and on Muostakh Island (Grigoriev, 2008). Based on this time-series, Muostakh is famous for very high rates of coastal thermo-erosion, where the northern end of the island for example retreated by about 25 m in 2005 and the nearby east-facing coast by 11 m (Fig. 2). Along with rapid erosion rates, the morphology of the coastal cliff may substantially change its appearance (Fig. 3).

3 Data and methods

3.1 Environmental parameters

We use environmental observations to relate coastal dynamics to its potential drivers of atmospheric warming and sea ice reduction. As a proxy for marine abrasion along the cliff bottom line, we use the inverse of sea ice coverage data, that is open water days (OWD). To identify single wind events during OWD that potentially enhanced coastal retreat we use wind data. To relate the rate of thaw along the cliff top line, we use air

TCD
7, 4101–4176, 2013

temperature (T_{air}) data as degree days thawing (DDT). These data are then used for correction of coastal erosion rates from different image acquisition periods.

3.1.1 Sea ice concentration data

Daily percent sea ice concentration and extent time series from 1992 to 2012, based on Special Sensor Microwave Imager (SSM/I) data distributed by Ifremer/CERSAT (2000), were used to calculate the open water fraction per day (OWD) in % d^{-1}. Derivation of total sea ice concentration from SSM/I data uses dual polarization measurements with the 19 and 37 GHz channels of 25 km spatial resolution. Higher resolution of 12.5 km is available with the 85.5 GHz channel. We worked with the 25 km product of the NASA team algorithm, since the higher resolution product is affected by larger uncertainties over lower sea ice concentrations and open water and more sensitive to atmospheric effects during arctic summer (Lomax et al., 1995; Lubin et al., 1997). Over or under-estimations of the higher resolution data are mainly observed in the marginal ice zone (Spreen et al., 2008). Also, Laptev Sea land fast ice, which extends up to 200 km off the coast, has very low backscatter values because of a lack of deformation structures, as described by Eicken et al. (2005). However, due to the coarse data resolution of 25 km, large areas of open water in the coastal zone might be blurred at subpixel scale (Markus and Burns, 1995), which in our study could correspond, for example to Tiksi Bay. In very few cases, the data can also accept negative and positive values outside the 0 – 100 % range (Andersen et al., 2007), requiring correction. Sea ice coverage was masked by land mass and limited to a 100 km radius around the northern end of Muostakh Island, spatially corresponding to mean sea ice concentration or open water fraction of the Buor Khaya Gulf. Daily sea ice coverage was smoothed using a 7 day running mean.

TCD
7, 4101–4176, 2013

3.1.2 Air temperature data

The spring to fall seasonal cycle in the Lena Delta region features rising T_{air} during spring until the end of snow melt, T_{air} well above the freezing point during summer, while fall is characterized by the beginning of refreeze (Langer et al., 2011). In order to evaluate the response of TD to T_{air} over time, we use the degree day approach, which combines the range and duration of T_{air} above or below a threshold and has been frequently applied as an index in permafrost studies from local to continental scales (Thompson, 1963; Smith and Riseborough, 2002; Etzelmüller et al., 2011). The hydrometeorological observatory at Tiksi, Russia (71.58° N, 128.92° E) has measured T_{air} every 3 h from 1932 until 2007. The station became a World Meteorological Station in 2010, and synchronous T_{air} data are available from 1999 until the present. For the historical erosion observation time range from 1951 to 2012, thawing degree days (DDT) were calculated using mean daily T_{air} data as annual sums and as cumulative DDT over our observation periods. Cumulative annual DDT was calculated as:

$$\sum_{T>0}^{365} T\,d \tag{1}$$

where T is the mean daily T_{air} in °C and d represents a 1 day period.

3.1.3 Wind data

Wind blowing over open water generates waves breaking on the shoreface. Wave height and subsequent wave energy and erosion potential of thermo-abrasion (TA) is proportional to wind speed. Data on wind direction and speed in Tiksi are available from 1999 until 2012 and were examined for storm events according to the meteorological definition, where a storm is defined by wind speeds of 24.5 m s^{-1} or more, measuring 10 or higher on the Beaufort wind force scale. Based on wind speed measurements every six hours, mean daily wind speed was calculated and cumulative wind speed was caluclated for observations during the sea ice free period of a particular year.

TCD
7, 4101–4176, 2013

3.2 Local parameters

Permafrost is exclusively defined by temperature (Van Everdingen, 2005) and prone to thawing because its core element is the occurrence of ground ice. Ice-wedges constitute a large fraction of the subsurface volume. They extend in different generations and statigraphic units from the top of the permafrost to below sea level, and their size directly determines how much clastic material must be thawed and subsequently removed by coastal thermo-erosion. On Muostakh, they are syngenetic ice-wedges that formed more or less simultaneously with the sediment and grew in response to surface aggradation (French, 2007). Visually estimating macro ground ice content based on the fractional ice-wedge volume (for example, from photographs of the coastal cliff) is often complicated by slope and perspective, by debris material that obscures undisturbed in-situ material, as well as by the fact that collapse of thermo-abrasional cliffs occurs along ice-wedge axes (Are, 1988b), implying that an exposed wall of ice may not serve as a representative random test for the geological subsurface.

3.2.1 Macro ground ice calculation

Baydzharakhs are a characteristic ephemeral cone-shaped thermokarst landform and represent the remnant frozen sediment core and geometric centers of thawed ice-wedge polygons (Yershov, 2004; Mudrov, 2007). During field work in 2011, twenty coastal slope profiles were surveyed between and across baydzharakhs at different locations, where we observed that baydzharakh densities varied and might do so depending on their fractional volume of the subsurface (Fig. 4).

Using ortho-rectified satellite imagery, we extended baydzharakh mapping to the entire cliff of erosional coast segments (Fig. 5). Taking mapped baydzharakh centers as seeds, we subdivided the surface into Voronoi cells (Reem, 2010), which we use as an estimate of polygon morphology prior to thaw. The largest possible circle within a cell was calculated using the maximum Euclidean distance of each cell as radius. Based on the assumption that the sediment center of each polygon has a cylindric

TCD
7, 4101–4176, 2013

form, macro ground ice content as fractional volume (V_{wm}) is calculated from

$$V_{wm} = 1 - \frac{A_{circle}}{A_{polygon}} \quad (2)$$

where A_{circle} is the surface of the sediment center in m^2 and $A_{polygon}$ total polygon area in plan in m^2. The resulting value is then assigned to the linearized edges of a polygon, representing the ice-wedge's main axis, to serve as contour lines for interpolation of macro ground ice content over the slope.

3.2.2 Subsidence potential calculation

According to Katasonov (2009), the porosity of Ice Complex deposits is very large, due to excess ice and fine particle size. However, natural sediment deposition forms cavities, and this fraction of the total porosity due to excess ice must be disregarded in terms of subsidence. We therefore assume a porosity of 0.4, following

$$\phi = 1 - \frac{\rho}{\rho_O} \quad (3)$$

where ρ is mean bulk density of Ice Complex on Muostakh of $1.6 \pm 0.25 \times 10^3\,kg\,m^{-3}$, according to Solomatin (1965) and ρ_O the particle density of non-porous clastic material ($2.6510^3\,kg\,m^{-3}$, J. Strauss, personal communication, 2013). Assuming that all pores are filled with ice (Strauss et al., 2012), the pore ice fraction of intrasedimentary ice does not contribute to subsidence. Therefore, the relative subsidence potential of thawing Ice Complex deposits was calculated following:

$$\delta z = V_{wm} + (V_s \cdot W_{is}) - (V_s \cdot W_{is} \cdot \phi) \quad (4)$$

modified after Mackay (1966) and Are (2012), where V_{wm} is volumetric macro ground ice content, V_s the volume of the sediment part, W_{is} intrasedimentary ground ice and ϕ the porosity.

TCD
7, 4101–4176, 2013

3.3 Field survey

During a joint Russian–German expedition to Muostakh in August 2011, a network of well distributed geodetic anchor points was established across the entire island as a precondition for consistent repeat topographic surveys and their transformation to an absolute coordinate system. We used a ZEISS ELTA C30 tacheometer for distance and height measurements. To ensure repeated surveys, we defined a local coordinate system and a network of well distributed anchor points was set up. For each anchor point, coordinates of an absolute coordinate system were collected using GPS waypoint averaging. All points of this network were marked with a measurement plastic plug in the ground. During a subsequent expedition in August 2012, a repeat survey was conducted along the eastern cliff top line. Elevation data were adjusted to sea level. Concentrated mainly along the erosive sections of the western and eastern coasts, 2392 points were measured that cover by about 2/3 of the island's 15 km cliff bottom coastline perimeter. In local project coordinates the point cloud was highly self-consistent, while the absolute geocoding accuracy had a root mean squared error (RMSE) of 1.36 m.

3.4 Data fusion and change detection for analzing coastal thermo-erosion development

Remote sensing data were acquired on different dates in order to create a time series of images that was integrated into a geographic information system (GIS), to detect and measure land loss resulting from coastline position changes. In this study, GIS serves as a basis for combining survey data from on-site geodetic measurements, historical aerial imagery, contemporary satellite images, and products generated from these data such as digital elevation models (DEM), ortho images, and digitization records.

The use of satellite images from different sensors with varying spatial, spectral, and radiometric properties represents challenges for change detection. This is especially true when using very high resolution image data with a ground resolution of < 1 m (Dowman et al., 2012), not only because pixel-based approaches have been designed for

TCD
7, 4101–4176, 2013

low to medium resolution imagery (Hussain et al., 2013), but specifically because of the different acquisition geometries that must be considered, requiring careful geometric rectification and topographic correction. Although our study area is flat tundra lowland, our main object of interest, the upper coastline, is always located on the sharp edge of coastal cliffs where abrupt elevation changes occur. In addition to temporally very dynamic elevation changes, steep thermo-abrasional cliffs and baydzharakhs on thermo-denudational coastal bluffs cause large dynamic shadow effects due to different illumination angles of the low solar elevation in high latitudes. Varying conditions of sea ice covered and sea ice free coastal waters, as well as the presence or absence of banks of snow at the cliff bottom, lead to large reflectance variabilities between acquisitions, making radiometric calibration almost impossible. These conditions lead to problems with automated change detection techniques, examples of which are given in Kääb et al. (2005).

Satellite images must be georeferenced for spatial calibration of multitemporal and multisensor data for change detection. While georeferencing corrects for most distortions connected with the acquisition system, orthorectification corrects for relief-induced displacement effects and creates calibrated satellite image products with the geometry of a map, allowing for distance and area measurements. In this local study, we therefore rely on our on-site reference measurements and manually digitize multitemporal coastline positions in orthorectified imagery to ensure their reliability and spatial context.

GIS related work is done using ESRI ArcGIS 10.1. Cliff top line positions were mapped at different points in time. Unlike other studies on coastal thermo-erosion using the transect method (Günther et al., 2013), we derived vector data of areal land loss and subsequently calculated seasonal variations of TD. This approach is also used by Aguirre et al. (2008) and Tweedie et al. (2012) for monitoring changes along an arctic coastline of the Elson Lagoon near Barrow (Alaska) but on the basis of DGPS measurements. Cliff bottom line position changes are regarded as baselines for historical and subdecadal thermo-abrasion dynamics. We divide the studied coastline into 118

TCD
7, 4101–4176, 2013

segments of 50 m equal width, 29 of which are located along the western and 89 on the eastern coast. Normalization of eroded area by baseline length of each segment provides absolute coastal retreat in m and normalization over time rates in $m\,a^{-1}$. We use TD and TA to refer to the rates of coastline position change per year.

3.4.1 Aerotriangulation of historical air photo strip

Aerotriangulation, or block adjustment of a bundle of rays from object to image coordinates, is a standard method in photogrammetry (Konecny and Lehmann, 1984). Aerial photogrammetry is well-suited to quantify historical decadal scale temporal change (Kääb, 2008). Although coastal erosion studies in the East Siberian Arctic using early aerial photography are common (Grigoriev, 1993; Are, 1999; Lantuit et al., 2011a; Pizhankova, 2011), few use stereophotogrammetry, generally because image parameters for old aerial photos are unknown. Therefore, valuable elevation information available from these datasets still remain untapped.

Five airborne images covering Muostakh Island taken on 9 September 1951 along one flight strip were utilized in this study (Fig. 6). Hard copies of 180 mm × 180 mm edge length were scanned using a photogrammetric scanner at 14 µm scan resolution, corresponding to ≈ 0.4 m on the ground. No information on focal length, principal point offset and radial lens distortion is available. However, the latter two can be compensated to some extent with exterior orientation (spatial location of the projection center and cameras view direction), for which camera focal length is required (Jacobsen, 2001). Whether or not the correct focal length of the air survey camera is used, calculation of the flight altitude is necessary (Knizhnikov et al., 2004), which can be done by determining the scale of the frame photography. The scale number S_a of the frame photography was roughly estimated following

$$S_a = S_m \cdot \frac{d_m}{d_a} \quad (5)$$

TCD
7, 4101–4176, 2013

by measuring the same distance between two objects within the original photograph (d_a, [cm]) and on-screen (d_m, [cm]) within contemporary ortho-image with a map scale (S_m) set to 1 : 10 000. The resulting scale approximation of 1 : 28 000 is close to that of aerial photographs from 1949 used by Are (1999) for the Mamontov Klyk coast, probably flown with the same camera. Using the Aerial Photography model in OrthoEngine, we collected fiducial marks in each image to visually define the principal point, collected a set of 25 stereo GCPs and automatically computed over 850 tie points (TPs) using cross correlation for strip stabilization. Bundle block adjustment was performed iteratively with the focal lengths of air survey cameras that existed at that time according to Shcherbakov (1979). The best overall solution was achieved with a focal length of 100 mm (likely Liar-6, 104° wide angle lens, used for topographic medium scale mapping), yielding a RMSE for GCP locations of 2.4 m and TPs of 0.3 m. For the exterior orientation parameters, this corresponds to a flight altitude of around 2600 m, which is consistent with the theoretical flight height (h) of 2800 m calculated from the approximate photo scale following:

$$h = S_a \cdot c_k \quad (6)$$

where c_k is the focal length in [m]. An overview of the air survey strip stereo constellation shows along-track stereo and triple overlap situations, with base-to-height-ratios of 0.7 and 1.4, respectively, allowing for height parallax measurements and DEM extraction of steeper slopes as well as over flat terrain (Fig. 6). Vertical accuracy of the DEM was estimated to be 2.3 m, based on the difference of input and calculated elevations at stereo GCP locations. Rectangular corners of footprints verify nadir viewing geometry, with rotation angles roll and pitch $\leq 1°$. The image strip model was stable and did not result in overfitting outside the GCP cloud, an important precondition for reconstructing the former shape of the island and subsequent change detection. Based on the DEM of 1951, the aerial photographies were ortho-rectified and stitched together in a seamless ortho-mosaic of Muostakh.

TCD
7, 4101–4176, 2013

3.4.2 Multi-sensor block adjustment

Multi-sensor data fusion, in this study of GeoEye (GE), QuickBird (QB), WorldView-1 (WV-1) and WorldView-2 (WV-2), offers the opportunity to merge images collected from different satellites and different orbits in one triangulation process. According to Toutin (2004), the simultaneous solution of an entire image block offers several advantages, for example the number of ground control points (GCP) can be reduced, better relative accuracy between images can be obtained and finally more homogeneous ortho-images over large areas can be produced. We performed block adjustment and subsequent ortho-rectification using our own ground control within the Rational Functions model (RPC based) in PCI Geomatica's 2013 module OrthoEngine. Satellite sensor models described by rational polynomial coefficients (RPC) provide a high potential of simple and accurate geopositioning (Fraser et al., 2006), are ideally suited for block adjustment of narrow field of view sensors (Grodecki and Dial, 2003), but require some bias correction (Fraser and Ravanbakhsh, 2009), and generally serve only as an approximation of physical sensor models when orbital information is not provided in the metadata (Poli and Toutin, 2012).

Prior to further geometric processing, we applied single-sensor and single-date image fusion to QB, GE, and WV-2 imagery using the enhanced pan-sharpening method of Zhang (2004). Seven very high resolution images were acquired as Geo (GE) and Ortho-Ready (QB, WV-1 and WV-2) products (Tab. 1), with panchromatic (PAN) imagery resampled with sinusoidal kernels, for better representation of sharp features (Toutin, 2011). Due to varying moisture and illumination conditions between acquisitions, we found that not all GCPs collected in the field could be identified unambiguously in each image, resulting on average in about 4 GCPs per image. The RPC model is a viable alternative for rigorous sensor models (Cheng et al., 2003), and several studies show that the effect of the number of GCPs on 3-D RPC block adjustment is limited, yielding almost no further improvement, if configurations of more than 4 GCPs are used (Fraser and Ravanbakhsh, 2009; Aguilar et al., 2012). Based on our topographic refer-

TCD
7, 4101–4176, 2013

ence measurements, 37 elevation tie points (TPs) were additionally incorporated into the block, to achive higher redundancy in RPC bias correction and mainly to better align images to each other. The zero order polynomial turned out to be the most stable and best possible solution of the block, resulting in an overall absolute geopositioning accuracy of 1.12 m GCP RMSE, while across track (longitude) residuals were 0.53 m and along track (latitude) residuals 0.58 m, yielding a submetre accuracy within the entire block of 0.79 m.

According to Günther et al. (2013), the mutual RMSE of each dataset (Tab. 1) is then considered as relative georeferencing uncertainty in the determination of the cumulative uncertainty in coastline position, which results out of the combination of this error, the ground resolution, and the additional 2-D positional error introduced by the DEM used for ortho-rectification, depending on the incidence angle. Uncertainties in subsequent change rate calculation are also applied following Günther et al. (2013). Errors associated with change measurements over five periods between 15 June 2010 and 7 September 2012 are in the range of 0.56–0.65 m.

3.4.3 DEM generation and ortho-rectification

The satellite images of 2010 to 2012 have no along-track stereo partner. Radiometric similarities for multi-date single-sensor (e.g. QB–QB) and multi-date multi-sensor (e.g. WV-GE) constellations were evaluated with regard to stereoscopic interpretation. Epipolar image matching of GE acquired on 13 July 2010 and WV-1 acquired 26 d later resulted in visually good topography that required some DEM post-editing. However, the base-to-height ratio, which describes the distance on the ground between projection centers and affects the accuracy of height parallax measurements, could not be checked via image metadata. Through pan-sharpening of GE's near infrared band (0.45–0.8 µm) with the PAN band (0.78–0.92 µm wavelength), the spectral range was adjusted to WV-1 PAN imagery (0.38 to 0.88 µm) to achieve enhanced image matching. For the GE-WV-1 stereoscopy, the elevation residuals of 3-D TPs showed the least standard deviation between input and calculated elevations, which systematically un-

TCD
7, 4101–4176, 2013

derestimated heights by 4.7 m compared to our survey data. Errors in height parallax measurement result from imperfect matching and image quality such as lack of visible contrast and similarity (Nuth and Kääb, 2011), which is likely to occur in time-shifted across track stereoscopy. The systematic bias was corrected by adjusting the GE-WV-1 DEM to the master data of the topographic survey using a trend surface, comparable to the approach of Pieczonka et al. (2011).

Final DEM generation was performed on a hybrid vector-raster data basis. Contour lines from the stereoscopic DEM, cliff bottom and top lines (digitized in ellipsoid-based ortho-images considering geoid height offset of 4.95 m around Muostakh), and all point data of the 2011 and 2012 topographic field surveys (that are necessarily within the 2010 cliff top line extent), were incorporated into a terrain interpolation procedure according to Hutchinson and Gallant (2000). The final DEM features high detail and represents the island's state in the early summer of 2010. The vertical accuracy of the DEM at survey point locations was 0.3 m, therefore introducing ≤ 0.1 m 2-D positional uncertainty along the cliff top line through subsequent ortho-rectification, instead of ≤ 7.2 m random terrain displacement for each of the 2010 to 2012 images when using the initial RPC reference height of the image products.

4 Results

4.1 Environmental parameters

4.1.1 Open water days (OWD)

Open water days (OWD) in [% d^{-1}] were calculated based on SSM/I sea ice concentration data for the past 21 yr from 1992 to 2012 in order to understand basic characteristics and interannual variablity of sea ice in the Buor Khaya Gulf. Background noise present in the data was quantified as 11 ± 5.5 % d^{-1}, by evaluating the open water fraction from December until April, when the land fast ice zone can be assumed to

TCD
7, 4101–4176, 2013

be completely covered with sea ice, and the sea ice concentration of August, when the coastal waters can be assumed to be free of sea ice. The influence of the perennial Laptev Sea polynya (Reimnitz et al., 1994; Dmitrenko et al., 2005) on the open water data was excluded by taking 100 km as reference zone. Meier and Stroeve (2008) find SSM/I sea ice concentration data of 15 % matches with the sea ice edge location for the Laptev and East Siberian seas. Adding 11 %d^{-1} uncertainty due to underestimation, we assumed that days with < 26 %d^{-1} within 100 km to be OWD.

As first order approximation, we assumed the mean annual open water fraction as indicator for seasonal duration available for thermo-abrasion (TA). Over the past two decades, mean open water fraction in a 100 km radius around Muostakh Island was 32.1 %d^{-1}, corresponding to 117 OWD a^{-1} in the Buor Khaya Gulf, including break-up and freeze-up transition periods. Based on the < 26 %d^{-1} threshold, the core open water season is 81 ± 15.1 d a^{-1} long, with mean open water fraction of 91 %d^{-1}. The average open water season lasts from 21 July until 9 October (Fig. 7). The difference between 117 and 81 OWD probably reflects 36 d of sea ice drift. The open water season for the current investigation period 2010–2012 was 96 ± 2.5 d long and lasted from 11 July to 14 October. For example Fig. 8 shows Muostakh and the surrounding coastal waters during break-up on 5 July 2011, and according to our data, the open water season started 5 d later.

4.1.2 Wind

Wind speed data was cross checked with data on sea ice concentration for the 2010 to 2012 study period and for the decade before. During our current study period no storm occurred, while strong breezes with wind speeds ≥ 10 m s^{-1} were observed twice during the open water period of 2010, once in 2011, and not in 2012. Over the previous decade (1999–2009), two severe storm events occured in 2000 (11 & 13 on the Beaufort scale), one in 2002 (11), and one in 2003 (14), $\frac{3}{4}$ of which had northern direction, causing water level to rise in the Buor Khaya Gulf. Based on this short record, severe storm events during the open water season in the Buor Gulf can be expected to re-

TCD
7, 4101–4176, 2013

cur at most every 3 a. Our current study period falls into this storm gap. Cumulative mean daily wind velocities over the sea ice free periods of the 1999–2012 reference period were $427 \pm 66\,m\,s^{-1}$ (Fig. 7). For the current investigation period 2010 – 2012 cumulative mean seasonal wind speed was $452 \pm 28\,m\,s^{-1}$.

4.1.3 Degree days thawing

Time series of T_{air} in Tiksi were used to calculate DDT over the historical time period from 1951 to 2012. The mean seasonal duration based on the first and last occurence of positive mean daily T_{air} is 133 d, where the season accordingly starts around 17 May and ends on 27 September. However, during this period still days with negative mean daily T_{air} occur. Mean cumulative annual DDT over the last 61 a was 660°d and mean daily DDT was 5.9°d. Therefore, the number of days with positive mean T_{air} is 112. Accounting for the difference of 21 d and assuming a spring–fall partition coefficient of 1 : 3 according to Fig. 9, the season available for TD starts roughly on 1 June and ends on 21 September. Current seasonal and interannual variations of DDT from 2010 to 2012 showed mean cumulative DDT over the last 3 a was 922°d, with a mean of 7.3 DDT, corresponding to seasonal duration of 126 d (Fig. 9). In 2012, cumulative DDT reached 1010°d for the fist time exceeding 1000°d in the period of record and lasted 134 d.

4.2 Local parameters – ground ice & sediment budget

Average macro ground ice content in the subsurface was calculated as 44 ± 4.6 % ($n = 1264$) by volume. The sediment occupied 56 % of the ground volume. The gravimetric ground ice content of Ice Complex sediments on Muostakh is 108 wt%, according to Schirrmeister et al. (2011). Assuming different densities for ice and solid material according to Strauss et al. (2012), 76 % of the sediments volume is occupied by intrasedimentary ground ice. Combining these 43 % intrasedimentary and 44 % macro

TCD
7, 4101–4176, 2013

ground ice, altogether 87 % by volume of the geological subsurface on Muostakh is composed of ground ice.

We applied the concept of critical ice content of Are (2012), using the newly available information on topography and ground ice contents. The relative subsidence potential was calculated as $\delta z = 0.69$. According to field observations, the ice-poor surface layer was on average 0.7 m thick, the upper $\frac{2}{3}$ of which is the active layer. The surface layer was assumed to be mainly composed of peat and therefore has been deducted from the depth of Ice Complex section. For the northern part of the island, where the base of Ice Complex deposits was detected at 10 m below sea level (Kunitsky, 1989; Grigoriev, 1993) and cliff height is 21 m a.s.l., potential subsidence of the entire 30.3 m Ice Complex thickness equals 20.9 m. If the ground ice would completely melt out, the top of the remaining thawed material would be situated only 0.1 m a.s.l. As possible scenario for the southern part of the island, where no information on the lower Ice Complex boundary is available, we applied the subsidence factor ($\delta z = 0.69$) to the mean elevation of the island's east coast of 16.7 ± 2.7 m, deducted the surface layer, and assumed the Ice Complex base at sea level. Accordingly, potential subsidence is 11 m, resulting in a top thawed material 5 m a.s.l. Both scenarios demonstrate that thawing results in a much reduced volume of sediment to be removed from the cliff bottom by waves. In the first scenario, where subsidence would extend almost down to sea level, Are (2012) emphasizes that this would mean coastal thermo-erosion may procced almost exclusively based on its thermal component. But, since coastal erosion takes place so quickly, flooding outweighs thaw, and therefore the second scenario, with remaining sediment column of < 6.5 m.a.s.l. for a 21 m high cliff in the north, in reality should also be the case for the north.

In addition to subsidence, ground ice can result in thermo-erosional niches at the water level that undercut the ice-rich cliff. Their theoretical maximum depth is determined by ice-wedge polygon size (Hoque and Pollard, 2009). Further investigation of the Voronoi diagram was done with a subsample of ice-wedge polygons that are entirely surrounded by other polygons. As a result, each polygon has 5.6 neighbors on

TCD
7, 4101–4176, 2013

average, which roughly corresponds to the common hexagonal form of ice-wedge polygons (Christiansen, 2005; French, 2007). They have a mean edge length of 9 ± 4.8 m, occupy a mean area of 162 m^2, and have a mean diameter of 14.2 ± 2.2 m. Ice wedge polygon rows along the cliff bottom and top showed slightly higher macro ground ice contents of 43.5 ± 8.7 and 47.9 ± 9.9 vol.%, respectively, compared to 41.1 ± 8.5 vol.% of the middle row (Fig. 10).

4.3 Historical erosion development

The development of thermo-erosion on Muostakh and its shaping of the island was analyzed over a period of time of more than half a century. Starting with the first aerial photographs from 1951 and ending with the most recent GeoEye image of 2012, erosion was quantified. We concentrated on the eroding portion of the coastline, and analyzed areal land loss over 61 yr and the associated volumetric land losses over 59 yr in more detail within 118 coastline segments. Each segment corresponds to 50 m coastline length on the beach level. Squares used for symbolizing erosion over the historical time period in Fig. 11 (middle) show spatial distrubution of all studied coastline segments.

4.3.1 Volume changes & mass movements

The volume of Muostakh Island has decreased by 34 % between 1951 and 2010, based on volumes calculated for those years, as well as on multitemporal DEMs. This reduction results from erosion on all sides of the island, a levelling of the surface, and an overall surface degradation.

According to table 2, the mean annually eroded volume on Muostakh is 0.34 $\times 10^6$ m^3, corresponding to an annual sediment displacement of 0.12×10^3 t. The cumulative eroded volume within the studied coastal segments was 0.25×10^6 m^3, which means that nearly $\frac{3}{4}$ of coastal erosion that is actually taking place was recorded by our coastline subsample for further analyzes (Fig. 11). Within each of the the 50 m

TCD
7, 4101–4176, 2013

coastal segments, annually eroded volumes per segment varied broadly and were on average $-2100 \pm 3100\,m^3a^{-1}$. Very high values up to $-28\,000\,m^3a^{-1}$ were detected at the north cape. Generally eroded volumes were highly skewed towards smaller values of $\leq 2000\,m^3a^{-1}$ (Fig. 12), because most of the coastline is eroding more slowly and has a lower backshore height than the northern cape.

4.3.2 Surface elevation changes

The relative vertical uncertainty between the DEMs of 1951 and 2010 was 1.6 m. In addition to large elevation decreases along the eroded coastline, we observed subsidence across the island, mainly in the northern part, and on slopes surrounding the fragment of the alas basin (Fig. 11 right). The elevation difference raster was clipped to the interior of the cliff top area of 2010, in order to exclude the influence of coastal cliffs for further analyses of this phenomenon. The calculated mean elevation of Muostakh was 15.7 m a.s.l. in 1951 and 13.3 m a.s.l. in 2010. Based on these data, approximately half of the current island's interior subsided by at least 1.3 m (Tab. 3), while negative elevation changes in the northernmost part were up to 4 m over the last 59 yr.

4.3.3 Coastline changes

Thermo-abrasion (TA) was analyzed in a planimetric fashion over 61 yr, where the start and end points of the observation period are in early September, meaning there is no shift with respect to season.

Günther et al. (2013) found that TD and TA along Ice Complex coasts are interconnected: TA is the limiting component for coastal thermo-erosion intensity on the long-term scale. TA also better reflects the overall land-loss of the base area of the island. The base area extent of Muostakh in 1951 was $3.8\,km^2$. By 2012 it had shrunk by $-23.7\,\%$ to $2.9\,km^2$, which corresponds to a mean land loss of $-14\,700\,m^2\,a^{-1}$. Given Muostakh's 2012 cliff bottom line perimeter of 15.5 km, this corresponds to a mean coastline retreat rate due to TA of $-0.95\,m\,a^{-1}$, when examined for the entire island.

TCD
7, 4101–4176, 2013

Areal land loss was mapped within each of the 118 segments. Transformation of areal data to mean distance measurements was done individually via the baseline length of a particular segment. The uncertainty of cliff bottom position change is ± 1.7 m, for TA ± 0.04 m a^{-1}. Along the 5.8 km coastline covered by our segmentation (corresponding to formerly 6.4 km in 1951), absolute TA ranged from −13.3 to −439.2 m and with a mean of about −109.7 ± 80.6 m, whereas annual rates were in the range from −0.2 to −7.2 m a^{-1} with −1.8 ± 1.3 m a^{-1} mean. According to Fig. 12, the relative frequency of medium TA rates (−2 to −4 m a^{-1}) was somewhat higher than medium eroded volumes, suggesting that historical planimetric rates create a more dynamic picture of coastal thermo-erosion than eroded volumes. This means that the impact of coastal erosion in terms of mass transport is somewhat more evenly distributed along the coastline than is reflected in 2-D rates. The maximum cliff bottom line recession was −585 m over the past 61 yr, which is equivalent to −9.6 m a^{-1}. This occurred at the exposed northern cape of the island.

4.4 Current interannual and seasonal erosion development

Open water and positive T_{air} are unequal in duration and time of year (Fig. 13). In 2010, the first 2 images were acquired during ice melt and increasing mean daily T_{air} (15, 29 June). The 13 July 2010 image represents the T_{air} summer peak and marks the start of the open water season. The fourth image was acquired during open water season, when mean daily T_{air} had already begun to fall (8 August 2010). Together with the previous image, it completely spans a period when both TD and TA are active. The 2010 fall season was bracketed by the fourth and the fifth image, acquired in early 2011 during ice melt and rising T_{air}. The 7 September 2012 image, acquired at the peak of the open water season and falling T_{air}, together with the previous image, captured almost two complete seasonal cycles.

Cumulative DDT and cumultive OWD are correlated during this period (Fig. 14) and probably generally, since sea ice melt is driven to a great degree by heat exchange

TCD
7, 4101–4176, 2013

with the atmosphere. This means that we expect TD and TA to be correlated insofar as they are driven by DDT and OWD, respectively.

4.4.1 Current thermo-abrasion

We examined current dynamics of TA using GeoEye images of 13 July 2010 and 7 September 2012 as the image data set spanning the longest period of the recent past, for which the cliff bottom is free of snow. Cumulative areal land loss at cliff bottom for the entire island was $-50\,800\,m^2$, $-44\,400\,m^2$ (87 %) of which were detected within our 118 coastline segments for detailed study. During this period, mean TA was $-3.5 \pm 2.8\,m\,a^{-1}$. However, due to the strong seasonal constraints on the development of coastal thermo-erosion, the discrepancy between the start and end points of this period and the duration of the season when TD and TA are able to proceed, may result in an over or underestimation of rates. In this case, the time period between two acquisition dates is 2.15 yr, but in fact it extends over 2.63 open water seasons, resulting in an overestimation of 18 %. Instead of direct change rate calculation via 2.63 seasons, we corrected the 2.15 yr based TA rate using a season factor, derived from the ratio of 252 d of open water during the observation period and cumulative 289 d of open water over the entire 2010–2012 period. This permits us to calculate the actual coastal erosion over a particular period of time, since a purely seasonal duration-based correction would equal almost a normalization. As a result, current mean TA was $-3.1 \pm 2.5\,m\,a^{-1}$ (Fig. 15). Also the base area reduction of the entire island was examined, where we currently observed land loss of $-20\,700\,m^2\,a^{-1}$ during the last 3 yr.

Although the northern cape is eroding a different angle than the rest of the northeastern coastline, it has traditionally been of interest as it reflects the increasing distance between Cape Muostakh on the adjacent Bykovsky Peninsula and Muostakh Island. Between 13 July 2010 and 7 September 2012 the northern cape retreated at −45 m along the historical position change line, which corresponds to a seasonally corrected TA rate of $-18.2\,m\,a^{-1}$. At this location, additionally topographic survey data of the expeditions in 2011 and 2012 were available down to the cliff bottom (Fig. 16). Inter-

TCD
7, 4101–4176, 2013

annual variations in costline position change were large. Between 2010 and 2011, the northernmost point of the island retreated by only −4.3 m, while it was −39.4 m during the following period between the two subsequent expedition surveys. However, further away from the cape the opposite picture emerged. Little erosion erosion occured from 2011 until 2012 when compared to the previous period from 2010 to 2011. Due to these effects, we considered the surrounding 50 m coastline segment as the northern cape area where mean TA over the whole 2010 – 2012 observation period was $-11.5\,\mathrm{m\,a^{-1}}$, being still the most rapid erosion among the entire coast of Muostakh Island (Fig. 15). Also of note is erosion that occured between the survey in Aug 2012 and the GE image, acquired 3 weeks after on 7 September, where the northern cape eroded up to −7.9 m, because of block failure and collapse due to the deep thermo-niche that existed before in this area (Fig. 16).

4.4.2 Current thermo-denudation

Using a chronologically consecutive approach of frequent closely-spaced TD measurements, we identified seasonal variations for 2010 and interannual variations during the 2010–2012 period. Using intervals of 14 – 437 d, we dealt with the problem of incomparability of land loss measurements along the cliff top line. The first two consecutive periods 1 and 2 were both 14 d long, while mean absolute TD had doubled from −0.46 ± 0.49 in period 1 to −0.97 ± 0.51 m in period 2. Period 3 was even one half longer (26 d) and consequently absolute TD was −2.13 ± 0.95 m. Period 4, as the last period which extended over less than a year, absolute TD decreased to −1.84 ± 1.22 m, despite longer lasting duration of 324 d, 83 d of which still belong to the TD active season (50 in 2010, 33 in 2011). Period 5 showed mean absolute TD of −5.18 ± 2.88 m over 437 d, 201 d of which nevertheless fell into the TD active season. Cumulative areal land loss across all current periods was $-59\,400\,\mathrm{m^2}$. Absolute linearized land loss for all periods is shown in Fig. 17. In order to compare TD intensity across the purely seasonal periods (1–4), normalization through simple annualization failed, due to large overestimations when compared to their reference baseline of mean TD over

TCD
7, 4101–4176, 2013

the entire coastal erosion cycle (Fig. 17). According to Fig. 18, simple annualization resulted for example in mean TD of -29.9 ± 13.3 m a^{-1} during period 3, while the most rapid single value of −79.7 m a^{-1} was detected in period 1 at the northern cape.

Normalization of TD rates, based on specific cumulative DDT and OWD for a certain period, showed different results for both environmental parameters. OWD–normalized TD rates ranged from −0.3 to -6.5 m a^{-1} and were on average −3.6 ± 2.5 m a^{-1}. OWD-normalization of TD worked for periods that cover at least one sea ice cycle and for period 3, as the only period when TD and TA have proceeded unrestricted simultaneously. DDT-normalized rates ranged from −4.4 to −6.6 m a^{-1} and were on average −5.5 ± 0.6 m a^{-1}. The very low standard deviation of $\sigma = 0.7$ m a^{-1} compared to initially $\sigma = 11.1$ m a^{-1}, indicates a high degree of levelling between periods and proved TD dependency on T_{air}. Based on this finding, we further applied a season correction factor that accounts for the fraction of DDT season duration into TD rate calculation. The resulting season factor corrected rates were considered as the actual TD that had taken place. This was proven by the fact that, the reference annual erosion cycle 2010 (29 June 2010–28 June 2011) turned out to be not affected by the correction approach, since simply annualized and season factor corrected TD rates over 2010 were equal (Fig. 18). We found TD rates during summer (periods 2 & 3) were always more rapid −9.5 ± 4.6 m a^{-1} than during spring with −4.1 ± 4.3 m a^{-1} (period 1) and during fall with −1.4 ± 0.9 m a^{-1} (period 4). Analyzes of interannual variations revealed more rapid TD rates over 2010 of −4.8 ± 2.3 m a^{-1}, compared to −3.4 ± 1.9 m a^{-1} during 2011–2012.

Altogether, TD was −4.1 ± 2.0 m a^{-1} for the entire 2010 – 2012 study period (included into Fig. 18 as reference baseline for current TD) and showed a normal distribution with a shift towards more rapid rates compared to current TA, but with a narrower distribution for TD (Fig. 15). This disproportion has led us to assess the quality of current thermo-erosion using the Normalized Difference Thermo-erosion Index (NDTI) according to Günther et al. (2012). It turned out that, 75 % of the segments from 2010 to 2012 eroded under prevailing TD with an average NDTI of 0.36 ± 0.28, while the largest positive TD-indicating NDTI values were observed in the middle of the island,

TCD
7, 4101–4176, 2013

parallel along both, the western and eastern coast with NDTI of 0.53 ± 0.25. On the northeastern coast, where erosion is most rapid, NDTI varied around zero, meaning constant erosion of large volumes (Fig. 17 lower right).

Based on the observation of more rapid TD rates during warm mid summer and succesful normalization of TD rates through cumulative DDT, we related mean daily positive T_{air} to the season–corrected annualized current TD rates of all current observation periods. In addition, we applied this calculation to the historical (1951–2010, 1951–2012) and current (2010–2012) annualized TA rates. As a result, we found that a continuous increase of mean daily T_{air} by 1 °C throughout the TD active period is responsible for an acceleration of coastal erosion by $-1.2 \pm 0.55\,m\,a^{-1}$ (Fig. 19).

5 Discussion

5.1 Changes of environmental parameters

Our observations of the sea ice free season length generally match with data of Markus et al. (2009), who analyze nearly 3 decades of satellite passive microwave data, until 2007. They find "inner" melt length is 90.9 ± 14.4 d and "outer" melt length 111.2 ± 14.2 d for the Laptev/East Siberian seas. We found that the duration of the sea ice free season was 81 ± 15.1 d and that the duration of open water 117 d. Although our study also included all above average sea ice free seasons from 2005 to 2012, seasonal duration was always 9 % shorter compared to Markus et al. (2009). This is in agreement with Karklin and Karelin (2009), who describe melt onset on the outer shelf of the Laptev Sea from 5 to 10 June, while sea ice melting along the coast starts only at the end of June and is connected with river water influence. Based on our observations for the reference period from 1992 to 2012, the open water season starts on 20 July, and therefore probably earlier than for the long-term observations (1980–2005), since land fast ice cover only breaks up around 15 to 20 July (Karklin and Karelin, 2009). Despite the fact that interannual variations are considerable, they report that negative

TCD
7, 4101–4176, 2013

anomalies of earlier break-up became a rule from 1999 to 2005. Our data show a continuation and strengthening of this trend, parallel to rising T_{air}.

Unexpectedly, the recent lengthening of the sea ice free season by 15 d from 81 to 96 ± 2.5 d on average for the 2010–2012 period, was due to 10 d prolongation in early summer and 5 d later freeze-up within the Buor Khaya Gulf, which is in contrast to the general decadal trend for the Laptev/East Siberian seas of 3 d earlier melt and 7 d later freeze-up in the fall according to Markus et al. (2009). Overeem et al. (2011) show that open water duration along the Alaskan Beaufort Sea coastline has been increasing (from icy to ice-free) over decades to a century based on SSM/I ice cover calculations. The open water has increased more during the stormy fall season than in spring, and mostly along the coast.

In our case, most likely, the extension of seasonal duration is forced by the earlier spring flood and increasing Lena River river discharge, which is most intense in the southeastern Lena Delta channels flowing into Buor Khaya Gulf, while discharge in the west flowing channel decreases (Federova et al., 2009). Fresher water around the eastern Lena Delta promotes quicker freeze-up since the freezing point of the fresher surface water is higher. The warmer river water is obviously more likely to influence local seasonality via early break-up than later freeze-up. Both factors suggest that, in the bay-marine environment of the Buor Khaya Gulf, seasonal duration of open water might differ from the offshore zone. Even around Muostakh, spatial variations of sea ice conditions are pronounced, where according to satellite imagery the rapidly eroding east-facing coast can be completely free of ice (Fig. 8), while on the west-facing coast, towards protected Tiksi Bay, sea ice may persist. The waters west of the island are thus ice-covered for longer than in Buor Khaya Bay. Gukov (2001) quantifies the offset in breakup between the eastern and western sides of the island as 12 d.

Wind speeds at Tiksi range between 0 and 25 m s^{-1}. Strong winds with wind speeds exceeding 10 m s^{-1} occur almost exclusively during the winter months, when sea ice cover within 100 km of Muostakh exceeds 85 % (Fig. 13). Adding to this seasonal protection of the island from wind-driven wave action is the fact that almost all high wind

TCD
7, 4101–4176, 2013

speed events come from the southwest to south (Fig. 13). Even when ice-free, the maximum fetch south to southwestward of Muostakh is less than 50 km. In terms of heavy swells, earlier summer might have strong impacts on TA on Muostakh Island, since $\frac{3}{4}$ of those rare strong storms that were recorded during the open water season over last decade occurred at the end of June and in mid-July. All of these storms had northern direction, where Muostakh is exposed to nearly unlimited fetch. Due to the longer open water period from 2010 to 2012, the cumulative seasonal wind speed was slightly above the average for the reference decade and a half before.

The very warm summer of 2010, with a mean daily T_{air} of $7.7 \pm 5.3\,^{\circ}C$ during the DDT period (124 d), was also accompanied by high net radiation (Boike et al., 2013). In 2011, T_{air} was lower ($6.5 \pm 4.9\,^{\circ}C$ over 121 d), but winds were stronger (Fig. 7), enhancing the convective heat transfer and maintaining melt on ground ice exposures. According to Langer et al. (2011), wind speed in the Lena Delta features a diurnal pattern, with enhanced heat exchange during the day and lowered turbulence during the night. In the very warm summer of 2012, daily T_{air} was $7.5 \pm 4.7\,^{\circ}C$ over the 134 d long DDT period. Mean July T_{air} of 12.5 °C in 2010, 10.7 °C in 2011, and 11.5 °C in 2012, were higher than the long-term mean July T_{air} of 7.5 °C (1951–2012) and 7.9 °C during the previous decade (1999–2009). Thus not even the criterion for a subpolar climate, that T_{air} is below 10 °C in the warmest month (Neef, 1956), was met in Tiksi over the last 3 yr. According to that classification, the climate zone boundary has probably shifted northwards, and the study area belonged to the zone of cool continental climate.

5.2 Local controls

5.2.1 Macro ground ice as endogeneous factor

Our estimates of 87 % total volumetric ground ice content on Muostakh are slightly above previous specifications of 80 % (Are, 1988a; Slagoda, 2004). The euclidean distance mean diameter of the baydzharakh measured on the imagery was 11 ± 2.1 m, which is larger than that surveyed in the field, where the mean base diameter was

TCD
7, 4101–4176, 2013

7.2 ± 1.8 m. The difference can be explained by denudation that occurred during thawing and the incomplete uncovering of the baydzharakh. Also, since our polygon mapping approach allows polygon sediment centers to touch the polygon's boundary in places, mapped ice wedges may have zero width in places. Thus, our geomorphometric method probably overestimates polygon sediment center size, resulting in conservative assessments of macro ground ice content. Since Muostakh Ice Complex sediment is one of the most coarsely grained and poorly sorted examples of Ice Complex (Slagoda, 2004; Schirrmeister et al., 2011), baydzharakhs there are better preserved following thawing, in contrast to those elsewhere, which quickly slump or undergo transport (Are et al., 2005).

The shape of syngenetic ice-wedges in vertical plan often deviates from the ideal wedge form (Popov et al., 1985). Generally 2 to 4 rows of baydzharakhs could be observed between the top and the bottom of the slope. Our results imply that the syngenetic ice wedges have a vertical hourglass, with higher ice contents and ice wedge widths at the top and bottom of the slope, and probably below the sea level. This picture generally agrees with field observations, with the exception that ice-wedge width at the bottom showed roughly constant width and not increasing width. Field observations confirm that syngenetic ice-wedges on Muostakh Island are thickest at the top and bottom of the coastal exposure. The higher ice contents thus occur at the positions where we measure coastal erosion and are predisposed to favor intense coastline retreat as a result of warming (TD) and wave action (TA).

5.2.2 Terrain elevation changes

The volumetric content of ground ice in unconsolidated permafrost deposits in East Siberian coastal lowlands exceeds their pore volume in the thawed state (Yershov, 2004), and consequently subsidence results when thawing occurs. The mean subsidence of −2.4 m is not randomly or uniformly distributed across the island but varies with geomorphology. The vertical accuracy of the 1951 DEM was determined as 2.3 m based on input and output of stereo GCPs. Input height was derived from the modern

TCD
7, 4101–4176, 2013

survey data. Restricting the search matrix size for cross-correlation of the 1951 aerial photographs to an elevation maximum of 21 m resulted in an almost complete failure of height parallax measurements north of the alas. For this reason, we extended the search matrix size to 27 m. However, since the whole terrain of Muostakh may potentially be susceptible to subsidence or other causes of elevation change, no long-term reference height points were available, except for the already completely degraded surface of the alas bottom and the area in the southern part of the island around the former polar station. In these two places, elevation differences were positive, with 1.6 m on average. Therefore, no further adjustment of the DEMs was performed, since detected negative changes are already conservative. Furthermore, no aspect, slope, or height dependent bias in DEM difference could be identified according to the strategies of Nuth and Kääb (2011).

5.2.3 Causes for subsidence

Generally, subsidence occurs by thaw at the top of ice-rich permafrost and drainage of melt water. Coastal erosion on Muostakh Island maintains a steep hydrological gradient so that rapid drainage is favored. Increases in cumulative DDT result in deeper thaw (Mackay, 1995; Burn, 1998). In 2012, we saw the highest cumulative DDT value (1010 °d) for the entire T_{air} record. Accordingly, active layer depth on Muostakh in 2012 was on average 47 ± 19 cm (I. A. Yakshina, personal communication, 2013). This agrees with mean thaw depth of 49 cm at the end of August on Samoylov Island in the Lena Delta (Boike et al., 2013), although soil conditions on this Holocene river terrace (Zubrzycki et al., 2013) differ from that on yedoma surfaces. For the nearby Bykovsky Peninsula, where active layer thickness on yedoma uplands varies by climate zone, Fyodorov-Davydov et al. (2008) document mean seasonal thaw depth of 32 cm during 2003–2006. During these 4 yr, mean cumulative annual DDT was 670 °d, very close to the 1951–2012 long-term average of 660 °d, and therefore clearly below the average cumulative annual DDT for the last two decades of 727 °d, 775 °d for the last decade, and 922 °d for the last 3 yr, when thaw depth on yedoma surfaces obviously increased

TCD
7, 4101–4176, 2013

by 15 cm. Where deeper thaw encounters ice-rich basal soil horizons or ice-wedge tops, higher DDT results not in active layer deepening, but in subsidence. Since the upper Ice Complex is ice-rich, increased heat flow into the ground will cause the island to subside. We therefore suggest that the widespread occurrence of peat mounds that present mainly polygonal centres, is associated with subsidence of the surrounding terrain, rather than with frost heave.

Comparison of our on-site survey with elevation indications from the literature supports the observation of decreasing height of the island. Generally backshore elevation along the east coast ranges from 21 m a.s.l. in the north to 13 m a.s.l. in the south. Around the former polar station the mean elevation is 6 m a.s.l. Ivanov and Katasonova (1978) report that the height of the island gradually decreases toward the south from 26 to 6 m. Slagoda (2004) present profiles of Ice Complex sequences that reached up to 25 m a.s.l. Topographic maps based on aerial surveys showed the highest point of the island 25 m a.s.l. in 1982. Grigoriev (2008) presents data of continuous on-site visits since the 1990's and takes 22.6 m as reference height for the north cape of Muostakh Island. Although all former elevation indications refer to the north cape, it is unlikely that only this portion of the island had an elevation ≥ 25 m a.s.l. Based on the literature, subsidence has occurred mostly during the last 30 yr. However, our 3-D dataset spans 59 yr, and estimates of annual subsidence range from 2 cm a^{-1} over the entire area affected by negative terrain height changes in the island's interior to 7 cm a^{-1} in the north. This is of the same order of magnitude observed elsewhere for ice-rich permafrost (Overduin and Kane, 2006).

5.3 Relationship between historical and current erosion development

Recently, TA proceeded at -3.1 ± 2.5 m a^{-1} and was therefore 1.7 times more rapid over the past 3 years than the historical record with mean TA of -1.8 ± 1.3 m a^{-1}. This proportion is consistent with observations made by Günther et al. (2013), who find recent rates are 1.6 to 3 times more rapid than historical TD and TA along Ice Complex coastlines throughout the Laptev Sea. They report that TA accelerated from long-term

TCD
7, 4101–4176, 2013

$-3.3 \pm 1.2\,m\,a^{-1}$ to $-5.7 \pm 1.2\,m\,a^{-1}$ over the past few years. When examined over almost 200 km of Ice Complex coastline and the last 42 yr, they find long-term TA was $-1.9 \pm 1.5\,m\,a^{-1}$. However, Ice Complex degradation through thermokarst (e.g. Grosse et al., 2007; Morgenstern et al., 2011) led to varying coastal cliff morphologies in terms of the proportion of low lying alas basins to yedoma uplands. The Mamontov Klyk coast, bordering the Olenyok-Anabar Lowland (Schirrmeister et al., 2008), is the most similar to Muostakh Island. According to Günther et al. (2013), long-term TD rates along the Mamontov Klyk coast are $-2.1 \pm 1.2\,m\,a^{-1}$ and accelerated recently to $-4.6 \pm 1.2\,m\,a^{-1}$. Current TD rates during the 2010–2012 period on Muostakh were $-4.1 \pm 2.0\,m\,a^{-1}$ and therefore of the same order of magnitude. This suggests that, despite the annually repeating record-breaking erosion rates on the northern cape, coastal thermo-erosion on Muostakh is not exceptional for Ice Complex coasts in the Laptev Sea. Deviations from the mean can be attributed to local variations of macro ground ice content and exposure to environmental parameters such as to offshore or bay-marine environments. Nevertheless, Muostakh is a regional exception when compared to the nearby Bykovsky Peninsula, where mean rates are $-0.59\,m\,a^{-1}$ (Lantuit et al., 2011a) or the opposite side of Buor Khaya Gulf where they are $-0.55\,m\,a^{-1}$ (Günther et al., 2013).

Since its base area shrank by 23.7 % during the last 61 yr, Muostakh Island is likely to disappear as island within the next 200 yr. If the currently observed erosion rates continue, Muostakh Island is likely to disappear earlier within the next 140 yr. Examples for disappering Ice Complex islands on the Laptev Sea shelf exist. According to Gavrilov et al. (2003), the former islands Diomede, Semenovsky, and Vasilevsky have become sandbanks with frozen sediments located very close to the seafloor surface, where thermo-abrasion is still active and proceeds with approximate rates of -0.02 to $-0.27\,m\,a^{-1}$. The subsequent submergence of arctic islands results in shoals on the shallow arctic shelf, grounded sea ice pressure ridges (Reimnitz et al., 1994), and loss of island status, as happened to Dinkum Sands off the Alaskan Beaufort Sea coast (Reimnitz, 2005). Klyuev et al. (1981) report on the shape of Vasilievsky Island in 1823, where according to topographic surveys carried out at this time, the island had

TCD
7, 4101–4176, 2013

a length of 7.4 km and was 463 m wide, quite similar to Muostakh Island today. As on Muostakh Island, erosion on Vasilievsky Island was most intensive along its major axis. Because of its narrow shape, Vasilievsky Island broke into two parts and was quickly destroyed afterwards due to the unstable ground-ice-rich composition of the island and to the chaotic erosion with rates up to 100 $m\,a^{-1}$ that occurred from all sides until the island was completely destroyed in 1936 (Klyuev et al., 1981). Vasilievsky Island was located quite far offshore and exposed to larger fetch on all sides. Muostakh Island has a narrow central section where we measured TA on both the west-facing and east-facing coasts. On the west-facing side, historical and modern rates do not differ greatly ($-0.8 \pm 0.6\,m\,a^{-1}$). On the east-facing side, however, modern rates ($-2.3 \pm 1.8\,m\,a^{-1}$) are more than twice the historical mean ($-1.0 \pm 0.2\,m\,a^{-1}$). Changes to sea ice cover are probably affecting the east-facing coast more, since it is exposed to Buor Khaya Gulf's comparatively large fetch. Possible future break up of the island will probably occur at this location driven by erosion of the east side of the island.

5.4 Interannual and seasonal variability of erosion

In 2010, very rapid TD rates of $-4.8 \pm 2.3\,m\,a^{-1}$ were observed. Despite the very warm summer of 2012, unexpectedly, TD during the 2011–2012 period was not as high as in 2010, but slower at $-3.4 \pm 1.9\,m\,a^{-1}$. Figure 3 suggests that the coastal exposure undergoes cyclic geomorphologic changes from a high degree of exposed ground ice to an almost complete coverage of ground ice by thermal denudation debris within the 2010–2012 period. Remote sensing derived TD is also in agreement with TD from our on-site repeat surveys. According to this control data set TD was $-2.8\,m\,a^{-1}$ for 2.5 km of the northeastern coastline from August 2011 to August 2012. This indicates that, even under higher T_{air}, TD increases only as long as TA removes material from the cliff bottom and (re)establishes steep cliffs. For the entire 2010–2012 cycle we therefore suggest that, beginning in 2010 high DDT resulted in rapid TD, depositing thawed material and obscuring exposed ground ice, slowing subsequent TD.

TCD
7, 4101–4176, 2013

In 2011, during the very long open water season of 99 d, TA reworked the coastal cliff to predominant steep cliffs at the northeastern coast in summer 2012 (Fig. 20). According to our field observations, the main mechanism was block failure due to undercutting by thermo-niches, which probably formed during the strong wind events that occurred in the open water period in 2010 (Fig. 13). However, acccording to Wobus et al. (2011), thermo-niches develop even under quiet sea conditions. Even if they form during storms, the effect on erosion of high Ice Complex cliffs is combined with a certain delay and consequently not immediately measurable with remote sensing techniques. Maximum thermo-niche development is constrained by ice-wedge polygon size. The continuous presence of thermo-niches was observed in the field exclusively along the northeastern and eastern coast, where backshore height is ≤ 21 m and syngenetic ice-wedges generally stretch across the whole vertical section, indicating that block failure occurs along the vertical plane according to Hoque and Pollard (2009), which is confirmed by normalized differential thermo-erosion index (NDTI) values that vary around zero (Fig. 17 lower right). Given a mean ice-wedge polygon size of 14.2 ± 2.2 m and mean TA of $-4.4 \pm 2.3\,\mathrm{m\,a^{-1}}$, one complete coastal thermo-erosion cycle would last for 3 yr. Therefore, our observations captured one cycle within the 2010–2012 period. Around the northern cape, current TA was $-11.5\,\mathrm{m\,a^{-1}}$ for the corresponding 50 m coastline segment (the most rapid in Fig. 15), so that one complete block failure cycle takes roughly one year there. However, since current TA across all segments was found to be 1.7 times more rapid than the historical rate, TA accelerated from $-9.6\,\mathrm{m\,a^{-1}}$ since 1951 to $-18.2\,\mathrm{m\,a^{-1}}$ recently. In general, we suggest that coastal erosion rates are linked to geomorphology particularly through the macro ground ice content and its subsurface distribution.

The established dependency of coastal thermo-erosion on T_{air} and the seasonally varying intensity of thaw on coastal ice cliffs agrees with other observations. Grigoriev et al. (2006) link coastal dynamics of East Siberian coasts to changes in climatic and permafrost conditions. They find a positive correlation between coastal retreat rate and macro ground ice content, especially when air temperatures exceed +4 °C. In West

TCD
7, 4101–4176, 2013

Siberia, where massive ground ice occurs along the arctic coast, Vasiliev et al. (2006) find that coastal retreat was two times higher where ground ice content was at 45 %, when compared to places with only 25 %. Lantz and Kokelj (2008) studied retrogressive thaw slumps in the Mackenzie delta region and find consistently to increasing by 1.3 °C mean summer T_{air} a 1.4 times more rapid general slump growth and an almost doubling of the ground-ice-rich slump headwall retreat. Our data of currently 1.7 times more rapid TD is well in the middle of the acceleration observed by Lantz and Kokelj (2008) and almost equal to recently observed 1.6 times more rapid coastal erosion rates in the Laptev Sea region by Günther et al. (2013). Wobus et al. (2011) used time lapse photography to study thermo-erosion along Alaska's Beaufort Sea coast. They report thaw rates of 1 to 6 cm d^{-1} during spring, prior to sea ice break-up. During our periods 1 and 2 (15 June to July 2010), both lasting for 14 d, cliff top line retreat was 0.46 and 0.97 m, and mean daily temperature was 5.8 °C and 10.6 °C, respectively. This corresponds to thaw rates of 3 to 7 cm d^{-1}. Wobus et al. (2011) also observe acceleration after open water season begins, which is consistent to more rapid rates on Muostakh during period 3 (13 July to 8 August 2010), the only phase when TD and TA proceeded simultaneously, and thaw was on average 8 cm d^{-1}, and in places reached 17 cm d^{-1}, under daily T_{air} of 12.7 °C. Thaw was slowest during fall 2010 at 2 cm d^{-1}. Ravens et al. (2012) develope a niche and block erosion model for the Alaskan Beaufort Sea coast, and find a good match to observed erosion rates. Their model turned out to be sensitive primarily to meteorological parameters, not to sea ice extent. Although we did not account for sea surface temperature, our TD normalization efforts also clearly showed TD sensitivity to T_{air} rather than to OWD. However, future studies should extend high temporal and spatial resolution seasonal analyses to TA to better account for possible marine forcing.

TCD
7, 4101–4176, 2013

6 Conclusions

In this study, we found that continuous coastal erosion on Muostakh Island in the Buor Khaya Gulf of the Laptev Sea during the last 60 yr caused land loss of about 24 % of the island's area, while its volume shrank by 34 %. Muostakh is composed of Ice Complex permafrost deposits, of which up to 87 % of the subsurface is occupied by ground ice. This exposes the island to thermal disturbances from coastal erosion and seasonal thaw and subsidence, leading to further destruction of the island and its final disappearance, which we expect to take place 60 yr earlier than expected under recently changing environmental conditions. Subsidence of the island's surface ranged from -2 to $-7\,\mathrm{cm\,a^{-1}}$ over 59 yr. Average coastal erosion from 1951 to 2012 was $-1.8 \pm 1.3\,\mathrm{m\,a^{-1}}$; recent rates were 1.7 times more rapid at $-3.1 \pm 2.5\,\mathrm{m\,a^{-1}}$. The distance from the mainland has been increasing by $-9.6\,\mathrm{m\,a^{-1}}$; this value almost doubled during 2010–2012 to $-18.2\,\mathrm{m\,a^{-1}}$.

Our findings demonstrate that the currently higher intensities of the two coastal erosion processes, thermo-abrasion (TA) and thermo-denudation (TD), are controlled at least in part by the increasing open water season and summer air temperatures. The open water season from 81 open water days (OWD) on average for the past two decades on average by 15 OWD over the 2010–2012 observation period, and for example up to 99 OWD in 2011. Cumulative annual positive air temperature from 1951 to 2012 in the nearby town of Tiksi was 660 °d of thawing (DDT), strongly increased to 920 over the 2010–2012 observation period, and currently up to 1010 DDT in 2012. Accordingly, the seasonal duration available for thermally induced retreat of coastal ice cliffs has lengthened from 110 d on average to 127 d during 2010–2012, and currently up to 134 d in 2012.

We show that normalization of diverse TD rates ($\sigma = 11.1\,\mathrm{m\,a^{-1}}$) through cumulative DDT for each period decreases variability of TD rates across all sub-periods to $\sigma = 0.7\,\mathrm{m\,a^{-1}}$. Based on this finding, we propose that cliff-top coastline position change rate for short season time periods be corrected by a seasonal factor that is calculated

TCD
7, 4101–4176, 2013

from the ratio of the number of actual DDT and the DDT of the corresponding entire season. Based on a set of seasonally corrected observations, we suggest that coastal erosion (TD) on this Ice Complex coast increases by 1.2 m a^{-1} per 1 °C of mean DDT.

Currently observed interannual variations in coastal erosion rates are also related to local factors, such as macro ground ice content variation with depth. This affects the geomorphology of the coastal exposure and the development of thermo-niches, which depend on ice-wedge polygon size. A spatially varying cyclicity of generally 1 to 3 yr duration provides a mechanism for interconnecting TD and TA at this time scale.

TA is only active during the open water season, while TD can proceed throughout the summer. In June, when air temperatures rise and the mainland is already free of snow, mud flows from TD accumulate on top of snow at cliff bottom, while the adjacent sea is still covered with sea-ice, preventing TA. In late August, TD is slowed due to refreezing of the active layer and coastal slopes, while TA may still proceed until land fast sea ice develops. This results in a phase shift in TA and TD. Currently observed shifts in sea ice duration and air temperature results primarily in an increase in the overlap of the active seasons for TA and TD – the resulting simultaneity of both processes is more important than the extension of either active season, because the widely varying value domains of TD and TA align, leading to normalized differential thermo-erosion index (NDTI) values around zero, meaning most effective erosion of volumes and associated mass displacement.

Acknowledgements. We acknowledge the support of this research through the Potsdam Research Cluster for Georisk Analysis and Sustainability (PROGRESS). We are thankful for the logistical support of our partners from the Tiksi Hydrobase, the Lena Delta Reserve, and the Arctic and Antarctic Institute, St. Petersburg – Russian Federation. We would like to thank our colleagues I. A. Yakshina, A. N. Sandakov, and H. Meyer for the pleasent collaboration in the field.

TCD
7, 4101–4176, 2013

References

Aguilar, M. A., Aguilar, F. J., Saldaña, M. M., and Fernández, I.: Geopositioning accuracy assessment of GeoEye-1 panchromatic and multispectral imagery, Photogramm. Eng. Rem. S., 78, 247–257, 2012. 4117

Aguirre, A., Tweedie, C. E., Brown, J., and Gaylord, A.: Erosion of the barrow environmental observatory coastline 2003–2007, Northern Alaska, in: Proceedings of the Ninth International Conference on Permafrost, University of Alaska, Fairbanks, 29 June–3 July, edited by: Kane, D. L. and Hinkel, K. M., vol. 1, 7–12, 2008. 4114

Andersen, S. O. R., Tonboe, R., Kaleschke, L., Heygster, G., and Pedersen, L. T.: Intercomparison of passive microwave sea ice concentration retrievals over the high-concentration Arctic sea ice, J. Geophys. Res.-Oceans, 112, C08004, doi:10.1029/2006JC003543, 2007. 4109

Are, F.: The role of coastal retreat for sedimentation in the Laptev Sea, in: Land–Ocean Systems in the Siberian Arctic, edited by: Kassens, H., Bauch, H., Dmitrenko, I., Eicken, H., Hubberten, H.-W., Melles, M., Thiede, J., and Timokohov, L., Springer, 287–295, 1999. 4115, 4116

Are, F. E.: Thermal abrasion of sea coasts, Polar Geography and Geology, 12, 1–86, doi:10.1080/10889378809377343, from: Termoabraziya morskikh beregov, Moscow, Nauka, 1980, 158 pp., 1988a. 4103, 4104, 4131

Are, F. E.: Thermal abrasion of sea coasts, Polar Geography and Geology, 12, 87–157, doi:10.1080/10889378809377352, from: Termoabraziya morskikh beregov, Moscow, Nauka, 1980, 158 pp., 1988b. 4103, 4111

Are, F. E.: The contribution of shore thermoabrasion to the Laptev Sea sediment balance, in: Proceedings of the Seventh International Conference on Permafrost, Yellowknife, Canada, edited by: Lewcowicz, A. G. and Allard, M., 25–30, 1998. 4104

Are, F. E.: Razrushenie beregov arkticheskikh primorskikh nizmennostej (Coastal Erosion of the Arctic lowlands), Academic publishing house “Geo”, Novosibirsk, 2012. 4112, 4122

Are, F. E., Grigoriev, M. N., Hubberten, H.-W., and Rachold, V.: Using thermoterrace dimensions to calculate the coastal erosion rate, Geo-Mar. Lett., 25, 121–126, doi:10.1007/s00367-004-0193-y, 2005. 4132

Are, F. E., Reimnitz, E., Grigoriev, M., Hubberten, H.-W., and Rachold, V.: The influence of cryogenic processes on the erosional Arctic shoreface, J. Coastal Res., 24, 110–121, doi:10.2112/05-0573.1, 2008. 4104

TCD
7, 4101–4176, 2013

Arp, C. D., Jones, B. M., Schmutz, J. A., Urban, F. E., and Jorgenson, M. T.: Two mechanisms of aquatic and terrestrial habitat change along an Alaskan Arctic coastline, Polar Biol., 33, 1629–1640, doi:10.1007/s00300-010-0800-5, 2010. 4105

Atkinson, D. E.: Observed storminess patterns and trends in the circum-Arctic coastal regime, Geo-Mar. Lett., 25, 98–109, doi:10.1007/s00367-004-0191-0, 2005. 4105

Bauch, D., Hölemann, J. A., Nikulina, A., Wegner, C., Janout, M. A., Timokhov, L. A., and Kassens, H.: Correlation of river water and local sea-ice melting on the Laptev Sea shelf (Siberian Arctic), J. Geophys. Res.-Oceans, 118, 550–561, doi:10.1002/jgrc.20076, 2013. 4103

Bauch, H. A., Mueller-Lupp, T., Taldenkova, E., Spielhagen, R. F., Kassens, H., Grootes, P. M., Thiede, J., Heinemeier, J., and Petryashov, V. V.: Chronology of the Holocene transgression at the North Siberian margin, Global Planet. Change, 31, 125–139, doi:10.1016/S0921-8181(01)00116-3, 2001. 4107

Boike, J., Kattenstroth, B., Abramova, K., Bornemann, N., Chetverova, A., Fedorova, I., Fröb, K., Grigoriev, M., Grüber, M., Kutzbach, L., Langer, M., Minke, M., Muster, S., Piel, K., Pfeiffer, E.-M., Stoof, G., Westermann, S., Wischnewski, K., Wille, C., and Hubberten, H.-W.: Baseline characteristics of climate, permafrost and land cover from a new permafrost observatory in the Lena River Delta, Siberia (1998–2011), Biogeosciences, 10, 2105–2128, doi:10.5194/bg-10-2105-2013, 2013. 4131, 4133

Burn, C. R.: The response (1958–1997) of permafrost and near-surface ground temperatures to forest fire, Takhini River valley, southern Yukon territory, Can. J. Earth Sci., 35, 184–199, doi:10.1139/e97-105, 1998. 4133

Charkin, A. N., Dudarev, O. V., Semiletov, I. P., Kruhmalev, A. V., Vonk, J. E., Sánchez-García, L., Karlsson, E., and Gustafsson, Ö.: Seasonal and interannual variability of sedimentation and organic matter distribution in the Buor-Khaya Gulf: the primary recipient of input from Lena River and coastal erosion in the southeast Laptev Sea, Biogeosciences, 8, 2581–2594, doi:10.5194/bg-8-2581-2011, 2011. 4104

Cheng, P., Toutin, T., Zhang, Y., and Wood, M.: QuickBird: geometric correction, path and block processing and data fusion, Earth Observ. Magazin., 12, 24–30, 2003. 4117

Christiansen, H. H.: Thermal regime of ice-wedge cracking in Adventdalen, Svalbard, Permafrost Periglac., 16, 87–98, doi:10.1002/ppp.523, 2005. 4123

TCD
7, 4101–4176, 2013

Dallimore, S. R., Wolfe, S. A., and Solomon, S. M.: Influence of ground ice and permafrost on coastal evolution, Richard Island, Beaufort Sea coast, N. W. T., Can. J. Earth Sci., 33, 664–675, 1996. 4106

Dmitrenko, I. A., Tyshko, K. N., Kirillov, S. A., Eicken, H., Hölemann, J. A., and Kassens, H.: Impact of flaw polynyas on the hydrography of the Laptev Sea, Global Planet. Change, 48, 9–27, doi:10.1016/j.gloplacha.2004.12.016, 2005. 4120

Dowman, I., Jacobsen, K., Konecny, G., and Sandau, R.: High Resolution Optical Satellite Imagery, Whittles Publishing, Dunbeath, 2012. 4113

Eicken, H., Dmitrenko, I., Tyshko, K., Darovskikh, A., Dierking, W., Blahak, U., Groves, J., and Kassens, H.: Zonation of the Laptev Sea landfast ice cover and its importance in a frozen estuary, Global Planet. Change, 48, 55–83, doi:10.1016/j.gloplacha.2004.12.005, 2005. 4103, 4109

Etzelmüller, B., Schuler, T. V., Isaksen, K., Christiansen, H. H., Farbrot, H., and Benestad, R.: Modeling the temperature evolution of Svalbard permafrost during the 20th and 21st century, The Cryosphere, 5, 67–79, doi:10.5194/tc-5-67-2011, 2011. 4110

Federova, I. V., Bolshiyanov, D. Y., Makarov, A. S., Tretyakov, M. N., and Chetverova, A. A.: Sovremennoe gidrologicheskoe sostoyanie delty reki Leny (Current hydrological state of the Lena River delta), in: Sistema Morya Laptevykh i prilegayushchikh morey Arktiki (System of the Laptev Sea and the Adjacent Arctic Seas), edited by: Kassens, H., Lisitzin, A. P., Thiede, J., Polyakova, Y. I., Timokhov, L. A., and Frolov, I. E., chap. 2.8, Moscow University Press, Moscow, 278–291, 2009. 4130

Forbes, D. L. and Hansom, J. D.: Polar coasts, in: Treatise on Estuarine and Coastal Science, edited by: Wolanski, E. and McLusky, D., chap. 3.10, Academic Press, Waltham, 245–283, doi:10.1016/B978-0-12-374711-2.00312-0, 2011. 4103

Fraser, C., Dial, G., and Grodecki, J.: Sensor orientation via RPCs, ISPRS J. Photogramm., 60, 182–194, doi:10.1016/j.isprsjprs.2005.11.001, 2006. 4117

Fraser, C. S. and Ravanbakhsh, M.: Georeferencing accuracy of GeoEye-1 imagery, Photogramm. Eng. Rem. R., 75, 634–638, 2009. 4117

French, H. M.: The Periglacial Environment, John Wiley & Sons, Ltd., Chichester, 3. edn., 2007. 4111, 4123

Fyodorov-Davydov, D. G., Kholodov, A. L., Ostroumov, V. E., Kraev, G. N., and Sorokovikov, V. A.: Seasonal thaw of soils in the North Yakutian ecosystems, in: Proceed-

TCD
7, 4101–4176, 2013

ings of the Ninth International Conference on Permafrost, University of Alaska Fairbanks, 29 June–3 July, edited by: Kane, D. L. and Hinkel, K. M., vol. 1, 481–486, 2008. 4133
Gavrilov, A. V., Romanovskii, N. N., Romanovsky, V. E., Hubberten, H.-W., and Tumskoy, V. E.: Reconstruction of ice complex remnants on the eastern Siberian arctic shelf, Permafrost Periglac., 14, 187–198, doi:10.1002/ppp.450, 2003. 4107, 4135
Gavrilov, A. V., Romanovskii, N. N., and Hubberten, H.-W.: Paleogeographic scenario of the postglacial transgression on the Laptev Sea shelf, Kriosfera Zemli (Earth's Cryosphere), 10, 39–50, available at: http://www.izdatgeo.ru/pdf/krio/2006-1/39.pdf, 2006. 4107
Grigoriev, M. N.: Kriomorphogenez Ustevoy Oblasti Reki Leny (Cryomorphogenesis of the Lena River mouth area), Melnikov Permafrost Institute, Russian Academy of Sciences, Siberian Branch, Yakutsk, 1993. 4107, 4115, 4122
Grigoriev, M. N.: Kriomorphogenez i litodinamika pribrezhno-shelfovoi zony morei Vostochnoi Sibiri (Cryomorhogenesis and lithodynamics of the East Siberian near-shore shelf zone), habilitation thesis, Melnikov Permafrost Institute, Russian Academy of Sciences, Siberian Branch, Yakutsk, 2008. 4108, 4134
Grigoriev, M. N., Rachold, V., Schirrmeister, L., and Hubberten, H.-W.: Organic carbon input to the Arctic Seas through coastal erosion, in: The Organic Carbon Cycle in the Arctic Ocean: Present and Past, edited by: Stein, R. and Macdonald, R., chap. 2.3, Springer, Berlin, 37–65, 2004. 4104
Grigoriev, M. N., Razumov, S. O., Kunitzky, V. V., and Spektor, V. B.: Dinamika beregov vostochnykh arkticheskikh morey Rossii: Osnovnye faktory, zakonomernosti i tendencii (Dynamics of the Russian East Arctic Sea coast: major factors, regularities and tendencies), Kriosfera Zemli (Earth's Cryosphere), 10, 74–94, 2006. 4103, 4137
Grigoriev, M. N., Kunitsky, V. V., Chzhan, R. V., and Shepelev, V. V.: On the variation in geocryological, landscape and hydrological conditions in the Arctic zone of East Siberia in connection with climate warming, Geogr. Nat. Resour., 30, 101–106, doi:10.1016/j.gnr.2009.06.002, 2009. 4103
Grodecki, J. and Dial, G.: Block adjustment of high-resolution satellite images described by rational polynomials, Photogramm. Eng. Rem. S., 69, 59–68, 2003. 4117
Grosse, G., Schirrmeister, L., Siegert, C., Kunitsky, V. V., Slagoda, E. A., Andreev, A. A., and Dereviagyn, A. Y.: Geological and geomorphological evolution of a sedimentary periglacial landscape in Northeast Siberia during the Late Quaternary, Geomorphology, 86, 25–51, doi:10.1016/j.geomorph.2006.08.005, 2007. 4107, 4135

TCD
7, 4101–4176, 2013

Grosse, G., Romanovsky, V., Jorgenson, T., Anthony, K. W., Brown, J., and Overduin, P. P.: Vulnerability and feedbacks of permafrost to climate change, Eos Trans. AGU, 92, 73–74, doi:10.1029/2011EO090001, 2011. 4104

Gukov, A. Y.: Gidrobiologiya Ustevoy Oblasti Reki Leny (Hydrobiology of the Lena River Mouth Area), Nauchny Mir, Moscow, 2001. 4130

Günther, F., Overduin, P., Sandakov, A., Grosse, G., and Grigoriev, M.: Thermo-erosion along the Yedoma Coast of the Buor Khaya Peninsula, Laptev Sea, East Siberia, in: Proceedings of the Tenth International Conference on Permafrost, Salekhard, Yamal-Nenets Autonomous District, Russia, 25–29 June, 2012, edited by: Hinkel, K. M., vol. 1, International Contributions, 137–142, available at: http://epic.awi.de/30828/, 2012. 4128

Günther, F., Overduin, P. P., Sandakov, A. V., Grosse, G., and Grigoriev, M. N.: Short- and long-term thermo-erosion of ice-rich permafrost coasts in the Laptev Sea region, Biogeosciences, 10, 4297–4318, doi:10.5194/bg-10-4297-2013, 2013. 4103, 4114, 4118, 4124, 4134, 4135, 4138

Hoque, M. A. and Pollard, W. H.: Arctic coastal retreat through block failure, Can. Geotech. J., 46, 1103–1115, doi:10.1139/T09-058, 2009. 4122, 4137

Hussain, M., Chen, D., Cheng, A., Wei, H., and Stanley, D.: Change detection from remotely sensed images: from pixel-based to object-based approaches, ISPRS J. Photogramm., 80, 91–106, doi:10.1016/j.isprsjprs.2013.03.006, 2013. 4114

Hutchinson, M. F. and Gallant, J. C.: Digital elevation models and representation of terrain shape, in: Terrain Analysis: Principles and Applications, edited by: Wilson, J. P. and Gallant, J. C., chap. 2, Wiley, New York, 29–50, 2000. 4119

Ifremer/CERSAT: SSM/I user manual, Ifremer/CERSAT, Plouzane, France, available at: http://www.ifremer.fr/cersat, 2000. 4109

Ivanov, M. S. and Katasonova, E. G.: Osobennosti kriolitogennykh otlozhenii ostrova Muostakh (Pecularities of the cryolithogenic deposits on Muostakh), in: Geokriologicheskie i gidrogeologicheskie issledovaniya Yakutii (Geocryological and Hydrogeological Investigations in Yakutia), Mel'nikov Permafrost Institute, Yakutsk, 1978. 4134

Jacobsen, K.: Direct georeferencing – exterior orientation parameters, Photogramm. Eng. Rem. S., 67, 1321–1332, 2001. 4115

Jones, B. M., Arp, C. D., Beck, R. A., Grosse, G., Webster, J. M., and Urban, F. E.: Erosional history of Cape Halkett and contemporary monitoring of bluff retreat, Beaufort Sea coast, Alaska, Polar Geogr., 32, 129–142, doi:10.1080/10889370903486449, 2009a. 4105

TCD
7, 4101–4176, 2013

Jones, B. M., Arp, C. D., Jorgenson, M. T., Hinkel, K. M., Schmutz, J. A., and Flint, P. L.: Increase in the rate and uniformity of coastline erosion in Arctic Alaska, Geophys. Res. Lett., 36, L03503, doi:10.1029/2008GL036205, 2009b. 4105

Jorgenson, M. T. and Brown, J.: Classification of the Alaskan Beaufort Sea Coast and estimation of carbon and sediment inputs from coastal erosion, Geo-Mar. Lett., 25, 69–80, doi:10.1007/s00367-004-0188-8, 2005. 4104

Kääb, A.: Remote sensing of permafrost-related problems and hazards, Permafrost Periglac., 19, 107–136, doi:10.1002/ppp.619, 2008. 4104, 4115

Kääb, A., Huggel, C., Fischer, L., Guex, S., Paul, F., Roer, I., Salzmann, N., Schlaefli, S., Schmutz, K., Schneider, D., Strozzi, T., and Weidmann, Y.: Remote sensing of glacier- and permafrost-related hazards in high mountains: an overview, Nat. Hazards Earth Syst. Sci., 5, 527–554, doi:10.5194/nhess-5-527-2005, 2005. 4114

Karklin, V. P. and Karelin, I. D.: Sezonnaya i mnogoletnyaya izmenchivost kharakteristik ledovogo rezhima morey Laptevykh i Vostochno-Sibirskogo (Seasonal and long-term variability of the ice conditions in the Laptev and East Siberian seas), in: Sistema Morya Laptevykh i prilegayushchikh morey Arktiki (System of the Laptev Sea and the Adjacent Arctic Seas), edited by Kassens, H., Lisitzin, A. P., Thiede, J., Polyakova, Y. I., Timokhov, L. A., and Frolov, I. E., chap. 2.2, Moscow University Press, Moscow, 187–201, 2009. 4129

Katasonov, E. M.: Litologiya merzlykh chetvertichnykh otlozhenii (kriolitologiya) Yanskoi Primorskoi Nizmennosti (Lithology of Frozen Quaternary Deposits (Cryolithology) of the Yana Coastal Plain), OAO PNIIIS, 2009. 4112

Klyuev, Y. V., Kotyukh, A. A., and Olenina, N. V.: Kartografo-gidrograficheskaya interpretatsia ischesnoveniya v More Laptevykh ostrovov Semenovskogo i Vasilievskogo (Cartographic-hydrographical Interpretation of Vanishing of the Islands Vasilievsky and Semenovsky in the Laptev Sea), Izvestiya vsesoyuznogo geograficheskogo obshchestva (Bulletin of the all-union Geographical Society), 6, 485–492, 1981. 4135, 4136

Knizhnikov, Y. F., Kravtsova, V. I., Baldina, E. E., Gel'man, R. N., Zinchuk, N. N., Zolotarev, E. A., Labutina, I. A., Khar'kovets, E. G., and Kotseruba, A. D.: Tsifrovaya stereoskopicheskaya model' mestnosti: Experimental'nye issledobvaniya (Digital Stereoscopic Terrain Model: Experimental Investigations), Nauchny Mir, Moscow, 2004. 4115

Konecny, G. and Lehmann, G.: Photogrammetrie, Walter de Gruyter, Berlin, New York, 4. edn., 1984. 4115

TCD
7, 4101–4176, 2013

Konishchev, V. N.: Paleotemperaturnye usloviya formirovaniya i deformacii sloev Ledovogo Kompleksa (Paleotemperature conditions of formation and deformation of Ice Complex layers), Kriosfera Zemli (Earth's Cryosphere), 6, 17–24, 2002. 4108

Kunitsky, V. V.: Kriolitologiya Nizovya Leny (Cryolithology of the Lower Lena), Melnikov Permafrost Institute, Russian Academy of Sciences, Siberian Branch, Yakutsk, 1989. 4107, 4108, 4122

Langer, M., Westermann, S., Muster, S., Piel, K., and Boike, J.: The surface energy balance of a polygonal tundra site in northern Siberia – Part 1: Spring to fall, The Cryosphere, 5, 151–171, doi:10.5194/tc-5-151-2011, 2011. 4110, 4131

Lantuit, H., Atkinson, D., Overduin, P. P., Grigoriev, M., Rachold, V., Grosse, G., and Hubberten, H.-W.: Coastal erosion dynamics on the permafrost-dominated Bykovsky Peninsula, north Siberia, 1951–2006, Polar Res., 30, 7341, doi:10.3402/polar.v30i0.7341, 2011a. 4105, 4115, 4135

Lantuit, H., Overduin, P. P., Couture, N., Wetterich, S., Aré, F., Atkinson, D., Brown, J., Cherkashov, G., Drozdov, D., Forbes, D. L., Graves-Gaylord, A., Grigoriev, M., Hubberten, H.-W., Jordan, J., Jorgenson, T., Ødegård, R. S., Ogorodov, S., Pollard, W. H., Rachold, V., Sedenko, S., Solomon, S., Steenhuisen, F., Streletskaya, I., and Vasiliev, A.: The arctic coastal dynamics database: a new classification scheme and statistics on arctic permafrost coastlines, Estuar. Coast., 35, 383–400, doi:10.1007/s12237-010-9362-6, 2011b. 4105

Lantz, T. C. and Kokelj, S. V.: Increasing rates of retrogressive thaw slump activity in the Mackenzie Delta region, N. W. T., Canada, Geophys. Res. Lett., 35, L06502, doi:10.1029/2007GL032433, 2008. 4138

Lomax, A. S., Lubin, D., and Whritner, R. H.: The potential for interpreting total and multi-year ice concentrations in SSM/I 85.5 GHz imagery, Remote Sens. Environ., 54, 13–26, doi:10.1016/0034-4257(95)00082-C, 1995. 4109

Lubin, D., Garrity, C., Ramseier, R., and Whritner, R. H.: Total sea ice concentration retrieval from the SSM/I 85.5 GHz channels during the arctic summer, Remote Sens. Environ., 62, 63–76, doi:10.1016/S0034-4257(97)00081-3, 1997. 4109

Mackay, J. R.: Segregated epigenetic ice and slumps in permafrost, Mackenzie Delta area, N. W. T., Geographical Bulletin, 8, 59–80, 1966. 4112

Mackay, J. R.: Active layer changes (1968 to 1993) following the forest–tundra fire near Inuvik, N. W. T., Canada, Arctic Alpine Res., 27, 323–336, 1995. 4133

TCD
7, 4101–4176, 2013

Markus, T. and Burns, B. A.: A method to estimate subpixel-scale coastal polynyas with satellite passive microwave data, J. Geophys. Res.-Oceans, 100, 4473–4487, doi:10.1029/94JC02278, 1995. 4109

Markus, T., Stroeve, J. C., and Miller, J.: Recent changes in Arctic sea ice melt onset, freezeup, and melt season length, J. Geophys. Res.-Oceans, 114, C12024, doi:10.1029/2009JC005436, 2009. 4103, 4129, 4130

Meier, W. N. and Stroeve, J.: Comparison of sea-ice extent and ice-edge location estimates from passive microwave and enhanced-resolution scatterometer data, Ann. Glaciol., 48, 65–70, doi:10.3189/172756408784700743, 2008. 4120

Morgenstern, A., Grosse, G., Günther, F., Fedorova, I., and Schirrmeister, L.: Spatial analyses of thermokarst lakes and basins in Yedoma landscapes of the Lena Delta, The Cryosphere, 5, 849–867, doi:10.5194/tc-5-849-2011, 2011. 4135

Mudrov, Y. V. (Ed.): Merzlotnye yavleniya v kriolitozone ravnin i gor (Permafrost Phenomena in Mountain and Plain Cryolithozone – General Terms and Definitions), Nauchnyi Mir, Moscow, 2007. 4104, 4111

Neef, E.: Das Gesicht der Erde: mit einem ABC, Brockhaus, Leipzig, 1956. 4131

Nuth, C. and Kääb, A.: Co-registration and bias corrections of satellite elevation data sets for quantifying glacier thickness change, The Cryosphere, 5, 271–290, doi:10.5194/tc-5-271-2011, 2011. 4119, 4133

Ogorodov, S. A.: Rol' morskikh l'dov v dinamike rel'efa beregovoi zony (The Role of Sea Ice in Coastal Dynamics), Moscow University Press, Moscow, 2011. 4103

Overduin, P. P. and Kane, D. L.: Frost boils and soil ice content: field observations, Permafrost Periglac., 17, 291–307, doi:10.1002/ppp.567, 2006. 4134

Overduin, P. P., Hubberten, H.-W., Rachold, V., Romanovskii, N. N., and Grigoriev, M. N., Kasymskaya, M.: The evolution and degradation of coastal and offshore permafrost in the Laptev and East Siberian Seas during the last climatic cycle, in: Coastline Changes: Interrelation of Climate and Geological Processes, edited by: Harff, J., Hay, W. W., and Tetzlaff, D. M., vol. 426, The Geological Society of America Special Paper, 97–111, doi:10.1130/2007.2426(07), 2007. 4104

Overeem, I., Anderson, R. S., Wobus, C. W., Clow, G. D., Urban, F. E., and Matell, N.: Sea ice loss enhances wave action at the Arctic coast, Geophys. Res. Lett., 38, L17503, doi:10.1029/2011GL048681, 2011. 4130

TCD
7, 4101–4176, 2013

Pieczonka, T., Bolch, T., and Buchroithner, M.: Generation and evaluation of multitemporal digital terrain models of the Mt. Everest area from different optical sensors, ISPRS J. Photogramm Rem. S., 66, 927–940, doi:10.1016/j.isprsjprs.2011.07.003, 2011. 4119

Pizhankova, E. I.: Termodenudatsiya v beregovoi zone Lyakhovskikh Ostrovov – rezultaty deshifrirovaniya aerokosmicheskikh snimkov (Termodenudation in the coastal zone of the Lyakhovsky islands – interpretation of aerospace images), Kriosfera Zemli (Earth's Cryosphere), 15, 61–70, 2011. 4115

Poli, D. and Toutin, T.: Review of developments in geometric modelling for high resolution satellite pushbroom sensors, Photogramm. Rec., 27, 58–73, 2012. 4117

Popov, A. I., Rozenbaum, G. E., and Tumel, N. V.: Kriolitologiya (Cryolithology), Moscow State University publishing house, Moscow, 1985. 4132

Ravens, T., Jones, B., Zhang, J., Arp, C., and Schmutz, J.: Process-based coastal erosion modeling for drew point, North Slope, Alaska, J. Waterw. Port C.-ASCE, 138, 122–130, 2012. 4138

Reem, D.: The geometric stability of Voronoi diagrams with respect to small changes of the sites, in: Proceedings of the 27th Annual ACM Symposium on Computational Geometry (SoCG 2011), 254–263, 2010. 4111

Reimnitz, E.: Dinkum Sands – a recently foundered Arctic island, J. Coastal Res., 21, 274–280, doi:10.2112/04-0167.1, 2005. 4135

Reimnitz, E., Dethleff, D., and Nürnberg, D.: Contrasts in Arctic shelf sea-ice regimes and some implications: Beaufort Sea versus Laptev Sea, Mar. Geol., 119, 215–225, doi:10.1016/0025-3227(94)90182-1, 1994. 4120, 4135

Romanovskii, N. N., Hubberten, H.-W., Gavrilov, A. V., Tumskoy, V. E., Tipenko, G. S., Grigoriev, M. N., and Siegert, C.: Thermokarst and land-ocean interactions, Laptev Sea Region, Russia, Permafrost Periglac., 11, 137–152, doi:10.1002/1099-1530(200004/06)11:2<137::AID-PPP345>3.0.CO;2-L, 2000. 4103, 4107, 4108

Romanovsky, V. E., Drozdov, D. S., Oberman, N. G., Malkova, G. V., Kholodov, A. L., Marchenko, S. S., Moskalenko, N. G., Sergeev, D. O., Ukraintseva, N. G., Abramov, A. A., Gilichinsky, D. A., and Vasiliev, A. A.: Thermal state of permafrost in Russia, Permafrost Periglac., 21, 136–155, doi:10.1002/ppp.683, 2010. 4104, 4108

Schirrmeister, L., Siegert, C., Kunitsky, V., Grootes, P., and Erlenkeuser, H.: Late Quaternary ice-rich permafrost sequences as a paleoenvironmental archive for the Laptev Sea

TCD
7, 4101–4176, 2013

Region in northern Siberia, Int. J. Earth Sci. (Geologische Rundschau), 91, 154–167, doi:10.1007/s005310100205, 2002. 4107

Schirrmeister, L., Grosse, G., Kunitsky, V., Magens, D., Meyer, H., Dereviagin, A., Kuznetsova, T., Andreev, A., Babiy, O., Kienast, F., Grigoriev, M., Overduin, P. P., and Preusser, F.: Periglacial landscape evolution and environmental changes of Arctic lowland areas for the last 60 000 years (western Laptev Sea coast, Cape Mamontov Klyk), Polar Res., 27, 249–272, doi:10.1111/j.1751-8369.2008.00067.x, 2008. 4135

Schirrmeister, L., Kunitsky, V., Grosse, G., Wetterich, S., Meyer, H., Schwamborn, G., Babiy, O., Derevyagin, A., and Siegert, C.: Sedimentary characteristics and origin of the Late Pleistocene Ice Complex on north-east Siberian Arctic coastal lowlands and islands – a review, Quatern. Int., 241, 3–25, doi:10.1016/j.quaint.2010.04.004, 2011. 4121, 4132

Schirrmeister, L., Froese, D., Tumskoy, V., Grosse, G., and Wetterich, S.: Yedoma: late pleistocene ice-rich syngenetic permafrost of Beringia, in: The Encyclopedia of Quaternary Science, edited by: Elias, S. A., vol. 3, Amsterdam, Elsevier, 542–552, 2013. 4103

Shcherbakov, Y. E.: Raschet i konstruirovanie aerofotoapparatov (Calculation and Construction of Air Survey Cameras), vol. 2, Mashinostroenie, Moskva, 1979. 4116

Slagoda, E. A.: Kriolitogennye otlozheniya primorskoi ravniny morya Laptevykh: litologiya i mikromorfologiya (poluostrov Bykovskiy i ostrov Muostakh) – Cryolitogenic sediments of the Laptev Sea coastal lowland: lithology and micromorphology (Bykovsky Peninsula and Muostakh Island), Ekspress, Tyumen, 2004. 4107, 4108, 4131, 4132, 4134

Smith, M. W. and Riseborough, D. W.: Climate and the limits of permafrost: a zonal analysis, Permafrost Periglac., 13, 1–15, doi:10.1002/ppp.410, 2002. 4110

Solomatin, V. I.: O strukture poligonal'no-zhilnogo l'da (On the structure of polygonal veined ice), in: Podzemnyi led (Underground Ice), edited by: Popov, A. I., vol. 2, Moscow University Press, Moscow, 46–72, 1965. 4112

Spreen, G., Kaleschke, L., and Heygster, G.: Sea ice remote sensing using AMSR-E 89-GHz channels, J. Geophys. Res.-Oceans, 113, C02S03, doi:10.1029/2005JC003384, 2008. 4109

Steele, M., Ermold, W., and Zhang, J.: Arctic Ocean surface warming trends over the past 100 years, Geophys. Res. Lett., 35, L02614, doi:10.1029/2007GL031651, 2008. 4103

Strauss, J., Schirrmeister, L., Wetterich, S., Borchers, A., and Davydov, S. P.: Grain-size properties and organic-carbon stock of Yedoma Ice Complex permafrost from the Kolyma lowland, northeastern Siberia, Global Biogeochem. Cy., 26, GB3003, doi:10.1029/2011GB004104, 2012. 4112, 4121

TCD
7, 4101–4176, 2013

Thompson, H. A.: Air temperatures in Northern Canada with emphasis on freezing and thawing indexes, in: Proceedings of the First International Conference on Permafrost, Lafayette, 11–15 November 1963, 272–280, 1963. 4110

Toutin, T.: Spatiotriangulation With Multisensor VIR/SAR Images, IEEE T. Geosci. Remote, 42, 2096–2103, 2004. 4117

Toutin, T.: State-of-the-art of geometric correction of remote sensing data: a data fusion perspective, Int. J. Image Data F., 2, 3–35, 2011. 4117

Tweedie, C. E., Aguirre, A., Cody, R., Vargas, S., and Brown, J.: Spatial and temporal dynamics of erosion along the Elson Lagoon coastline near Barrow, Alaska (2002–2011), in: Proceedings of the Tenth International Conference on Permafrost, Salekhard, Yamal-Nenets Autonomous District, Russia, 25–29 June 2012, edited by: Hinkel, K. M., vol. 1: International Contributions, 425–430, 2012. 4114

Van Everdingen, R. (Ed.): Multi-Language Glossary of Permafrost and Related Ground-Ice Terms, National Snow and Ice Data Center/World Data Center for Glaciology, Boulder, CO, available at: http://nsidc.org/fgdc/glossary/ (last access: 15 September 2009), 2005. 4111

Vasiliev, A.: Permafrost controls of coastal dynamics at the Marre-Sale key site, western Yamal, in: Permafrost: proceedings of the 8th International Conference on Permafrost, Zürich, Switzerland, 21–25 July, edited by: Philips, M., Springman, S., and Arenson, L., vol. 2, 1173–1178, A. A. Balkema Publishers, Rotterdam, 2003. 4105, 4106

Vasiliev, A., Streletskaya, I., Cherkashev, G., and Vanshtein, B.: Coastal dynamics of the Kara Sea, Kriosfera Zemli (Earth's Cryosphere), 10, 56–67, 2006. 4105, 4138

Winterfeld, M., Schirrmeister, L., Grigoriev, M. N., Kunitsky, V. V., Andreev, A., Murray, A., and Overduin, P. P.: Coastal permafrost landscape development since the Late Pleistocene in the western Laptev Sea, Siberia, Boreas, 40, 697–713, doi:10.1111/j.1502-3885.2011.00203.x, 2011. 4104

Wobus, C., Anderson, R., Overeem, I., Matell, N., Clow, G., and Urban, F.: Thermal erosion of a permafrost coastline: improving process-based models using time-lapse photography, Arct. Antarct. Alp. Res., 43, 474–484, 2011. 4137, 4138

Yershov, E. D.: General Geocryology, Studies in Polar Research, Cambridge University Press, Cambridge, first published in Russian as Obshchaya Geokriologiya, by Nedra, 1990, 2004. 4111, 4132

Zhang, Y.: Understanding image fusion, Photogramm. Eng. Rem. S., 70, 657–661, 2004. 4117

TCD
7, 4101–4176, 2013

Zhigarev, L. A.: Osobennosti dinamiki beregovoi kriolitozony arkticheskikh morei (Pecularities of coastal cryolithozone dynamics of arctic seas), in: Dinamika arkticheskikh poberezhii Rossii (Dynamics of Russian Arctic Shores), Moscow State University publishing house, Moscow, 19–34, 1998. 4104

Zubrzycki, S., Kutzbach, L., Grosse, G., Desyatkin, A., and Pfeiffer, E.-M.: Organic carbon and total nitrogen stocks in soils of the Lena River Delta, Biogeosciences, 10, 3507–3524, doi:10.5194/bg-10-3507-2013, 2013. 4133

TCD
7, 4101–4176, 2013

Table 1. List of very high resolution optical remote sensing data used for change detection from 2010 to 2012 and summary of multi sensor bundle block adjustment parameters.

Sensor	Date	incidence angle [°]	Resolution [m]	No. of GCPs	No. of TPs	GCP RMSE [m]	TP RMSE [m]	RMSE [m]
QuickBird-2	23 May 2010	12	0.6	2	16	0.72	1.03	1.0
Quickbird-2	15 Jun 2010	15.3	0.6	3	22	0.88	0.73	0.75
WorldView-2	29 Jun 2010	18.8	0.5	3	18	1.08	0.72	0.78
GeoEye	13 Jul 2010	18.9	0.5	5	21	1.61	0.62	0.9
WorldView-1	8 Aug 2010	15.6	0.5	4	34	1.11	0.65	0.71
WorldView-1	28 Jun 2011	17	0.5	4	18	1.06	0.72	0.8
GeoEye	7 Sep 2012	14	0.5	6	17	0.77	0.53	0.6

TCD
7, 4101–4176, 2013

Table 2. Volumetric losses and associated mass displacement on Muostakh Island, based on DEMs from 1951 and 2010 for different compartments of the subsurface, assuming fractional volumes of 44 % macro ground ice and 43 % intrasedimentary ground ice.

	Muostakh 1951	Muostakh 2010	Total loss
Total volume [m^3]	$59.5 \pm 8.7 \times 10^6$	$39.3 \pm 0.9 \times 10^6$	$20.2 \pm 1.4 \times 10^6$
Surface layer [m^3]	2.4×10^6	1.9×10^6	0.5×10^6
Macro ground ice [m^3]	$25.1 \pm 4.3 \times 10^6$	$16.5 \pm 1.6 \times 10^6$	$8.6 \pm 0.9 \times 10^6$
Intrasedimentary ice [m^3]	$24.6 \pm 3.0 \times 10^6$	$15.9 \pm 1.1 \times 10^6$	$8.7 \pm 0.8 \times 10^6$
Clastic material [m^3]	$7.4 \pm 5.2 \times 10^6$	$5.0 \pm 1.9 \times 10^6$	$2.4 \pm 1.2 \times 10^6$
Total ground ice [t]	$45.6 \pm 4.7 \times 10^3$	$29.7 \pm 1.7 \times 10^3$	$15.9 \pm 1.1 \times 10^3$
Clastic material [t]	$19.6 \pm 8.3 \times 10^3$	$13.3 \pm 3.0 \times 10^3$	$6.3 \pm 1.9 \times 10^3$

TCD
7, 4101–4176, 2013

Table 3. Potential terrain subsidence of the undisturbed surface on Muostakh Island, examined using mean elevation of the island, and varying reference planes of DEM difference with respect to DEM matching.

Reference basis	Affected area of island interior [%]	Surface volume [m^3]	Elevation change [m]
DEM based mean m a.s.l.	–	–	−2.4
DEM difference above 0 m	32.5	0.7×10^6	1.1
DEM difference below 0 m	67.5	4.18×10^6	−2.1
DEM difference above 1.6 m	5.3	0.15×10^6	1.0
DEM difference below −1.6 m	46	1.61×10^6	−1.3

TCD
7, 4101–4176, 2013

Table 4. List of time periods used for coastal thermo-erosion change detection, bracketed by remote sensing data acquisitions. Periods referred to as letters correspond to observations covering more than one year. Thermo-abrasion (TA) observations along the cliff bottom line required correction for season fractions through open water days (OWD), while thermo-denudation (TD) was season-corrected using degree days thawing (DDT).

No. (type)	Time period	Land loss [m^2]	Erosion [m]	DDT	OWD [$\% d^{-1}$]	Season factor
A (TA)	9 Sep 1951–7 Sep 2012	735 000	109	40 260	–	1
B (TA)	13 Jul 2010–7 Sep 2012	44 000	7.6	2410	42.9	0.87
C (TD)	15 Jun 2010–7 Sep 2012	59 000	10.2	2584	42.1	0.89
D (TD)	29 Jun 2010–28 Jun 2011	27 300	4.8	937	37.7	1
1 (TD)	15 Jun–29 Jun 2010	2000	0.5	113	19.7	0.3
2 (TD)	29 Jun–13 Jul 2010	4300	1.0	158	61.4	0.3
3 (TD)	13 Jul–8 Aug 2010	12 400	2.1	308	95.6	0.3
4 (TD)	8 Aug 2010–28 Jun 2011	10 700	1.8	391	32	0.58
E (TD)	28 Jun 2011–7 Sep 2012	30 000	5.2	1614	46.6	0.83

TCD
7, 4101–4176, 2013

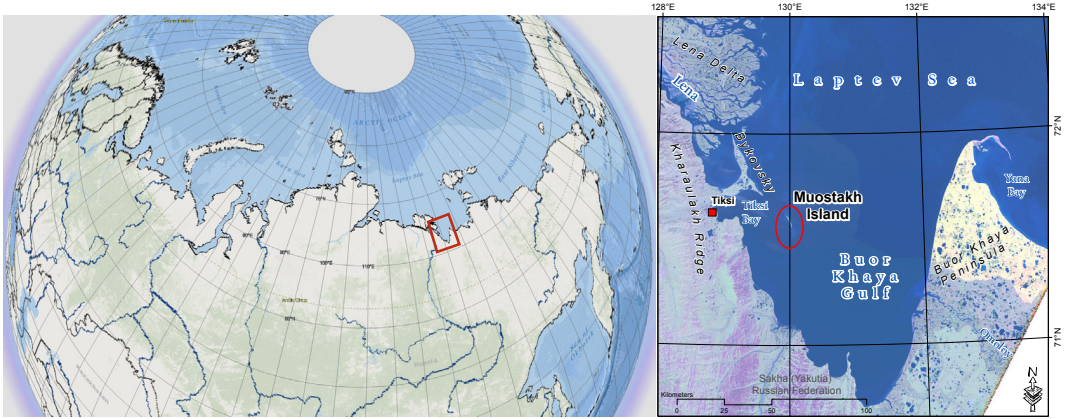

Fig. 1. Left: Situation of the map sheet in the north of East Siberia (source: ESRI); right: location of Muostakh Island within the Buor Khaya Gulf (September 2010 Landsat-5 imagery as background).

TCD
7, 4101–4176, 2013

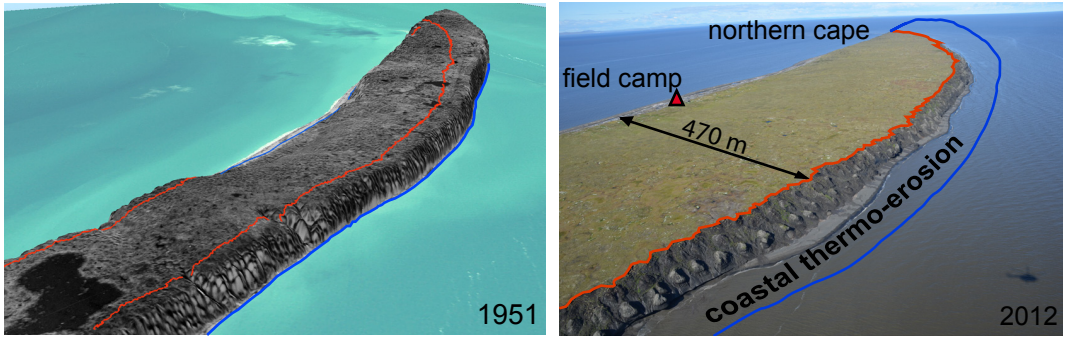

Fig. 2. Coastal thermo-erosion over time in the northern part of Muostakh Island. Historical cliff bottom (1951) and current cliff top line (2012) border the subaereal coastal thermo-erosion zone, where thermo-abrasion (blue, 1951 cliff bottom line) and termo-denudation (red, 2012 cliff top line) proceed. Left: orthophoto of historical aerial imagery draped over 1951 DEM with 5× superelevation. Note: the lake in the lower left has been drained during the observation period; right: oblique photograph taken from helicoper during the joint Russian–German expedition in August 2012. Location of 2011 and 2012 field camp in the alas floor, maximum island's width for scale.

TCD
7, 4101–4176, 2013

Fig. 3. Appearance of the 21 m high east coast close to the northern cape at the same season in two consecutive years. Upper photograph: debris flows covering coastal bluff in 2011 indicates TD surpassing TA, person for scale; lower photograph: nearly vertical ice-wall undercut by thermo-erosional niches in 2012 indicates TA surpassing TD.

TCD
7, 4101–4176, 2013

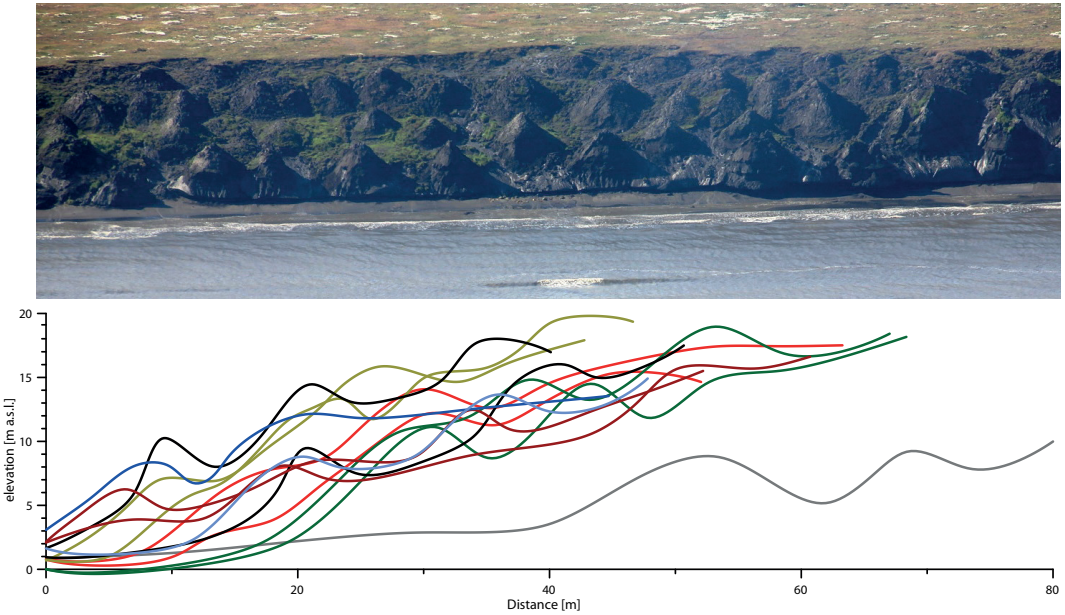

Fig. 4. Top: photograph of a baydzharakh field on the east coast of Muostakh Island, courtesy of I. A. Yakshina; Bottom: examples of slope profiles across baydzharakhs, showing differences in baydzharakh spacing. Profiles with same color coding were measured next to each other, no superelevation for height.

TCD
7, 4101–4176, 2013

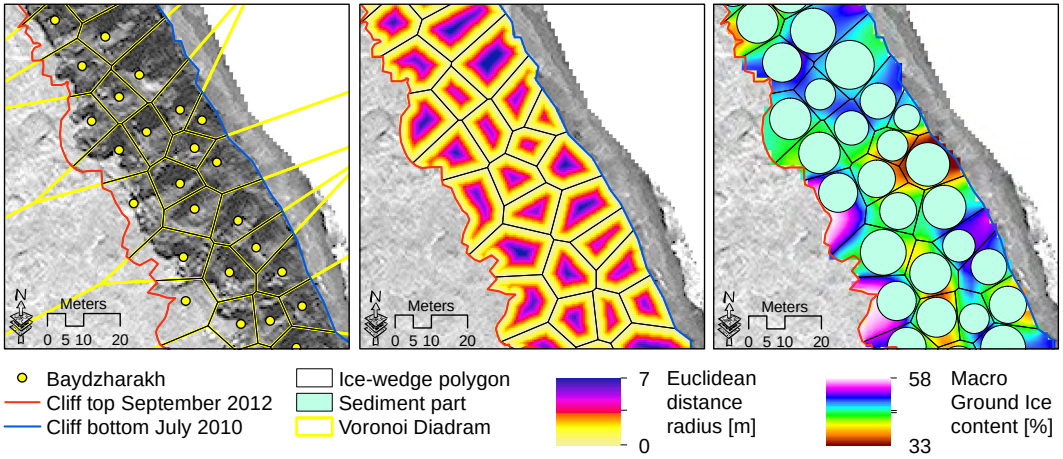

Fig. 5. Left: points mark mapped baydzharakh center locations, used for derivation of the Voronoi diagram, which was clipped to cliff top to bottom extent using digitized coastlines for polygon boundary differentiation; middle: determination of the euclidean distance within each polygon; right: construction of largest possible circles within a polygon using maximum euclidean distance as radius, representing the sediment component of the subsurface. Calculation and interpolation of macro ground ice content between circles based on the ratio of area occupied by circles and total polygon area (8 August 2010 WorldView-1 imagery as background).

TCD
7, 4101–4176, 2013

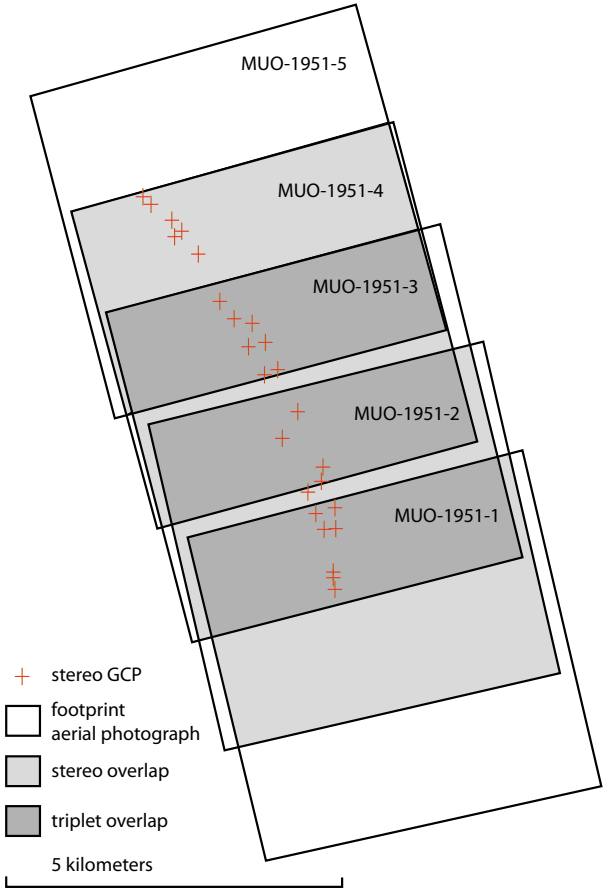

Fig. 6. Configuration of a flight strip of 5 aerial photographies from September 1951 over Muostakh Island and distribution of stereo GCPs.

TCD
7, 4101–4176, 2013

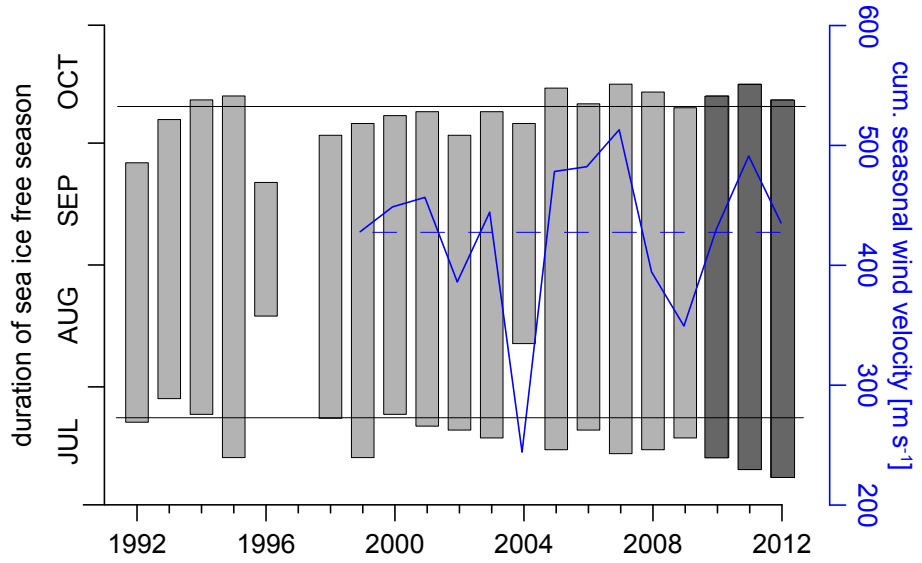

Fig. 7. Seasonal duration of the sea ice free period in the Buor Khaya Gulf. Upper and lower horizontal lines indicate mean start and end days according to the reference time period 1992–2012 with mean seasonal duration of 80 days. Cumulative seasonal mean daily wind speed for a particular year. Horizontal line indicates mean value of the 1999–2012 reference period.

TCD
7, 4101–4176, 2013

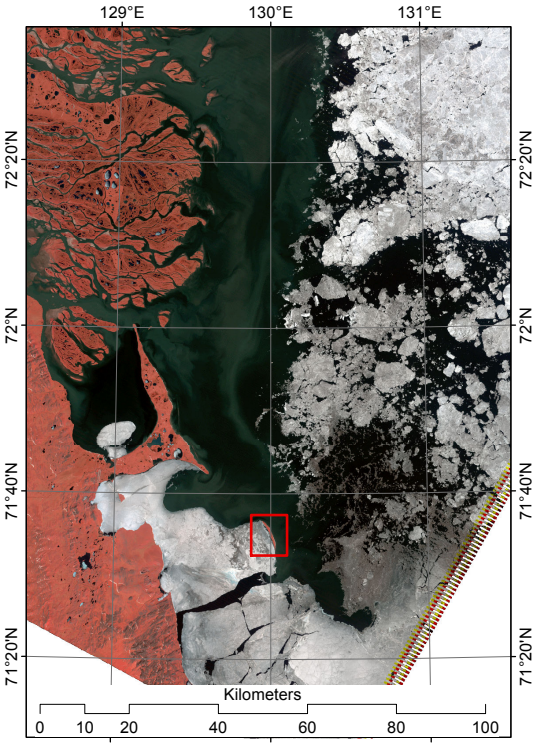

Fig. 8. Detail of a Landsat-5 image (4, 3, 2 CIR) showing the coastal waters around Muostakh Island (red square) and Bykovsky Peninsula southeast of the Lena Delta 4 July 2011. Note the coherent sea ice cover in Tiksi Bay and the open water adjacent to the Lena Delta. Open water fraction on this day 100 km around Muostakh Island was 62 %. Sea ice free season started 5 days after.

TCD
7, 4101–4176, 2013

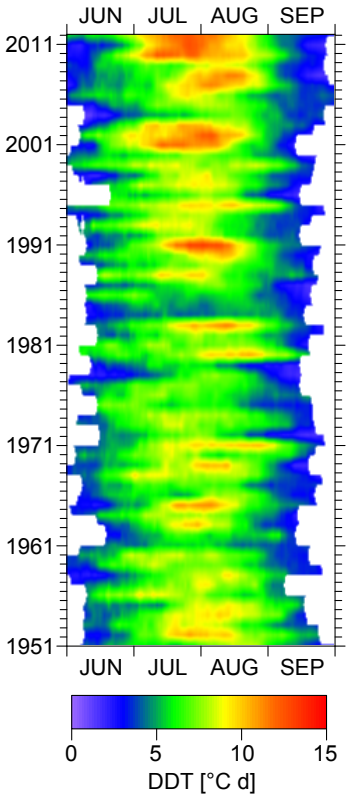

Fig. 9. DDT time series over the period from 1951 to 2012 show lengthening and intensification. Seasonal duration available for thermo-denudation lengthened from 112 days for the entire 61 yr period, to 126 days over the last three years (2010–2012). Simultaneously, mean DDT was currently 1.4°d higher and increased from 5.9 to 7.3°d.

TCD
7, 4101–4176, 2013

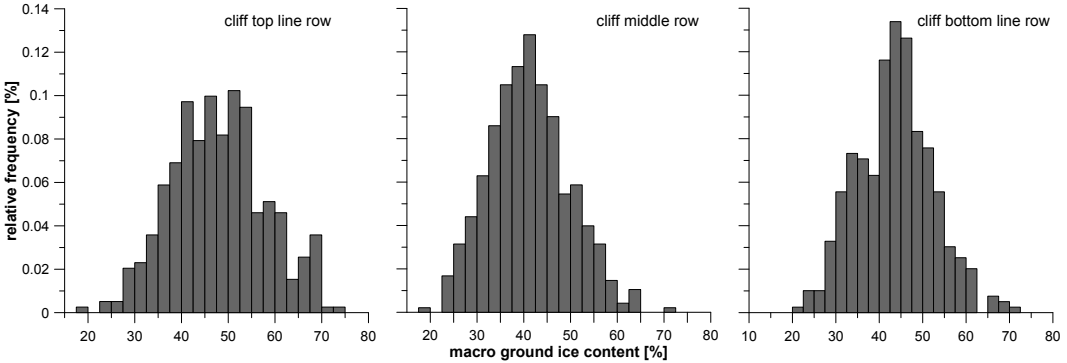

Fig. 10. Histograms of macro ground ice content along erosive coastal cliffs on Muostakh Island. Classification of ice-wedge polygons into three different vertical positions shows shift towards higher macro ground ice contents for the lower an upper part of the subsurface.

TCD
7, 4101–4176, 2013

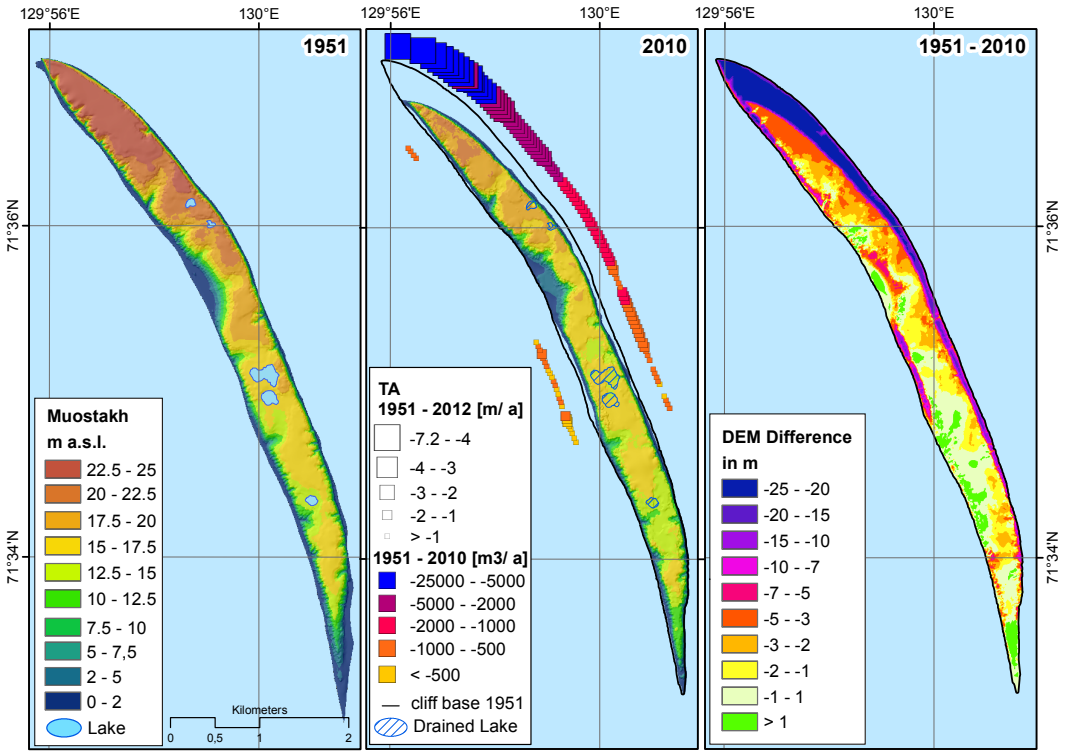

Fig. 11. Left: DEM from 1951 stereoscopic aerial photography; middle: hybrid DEM from topographic surveys and stereoscopic analyzes of GeoEye and WordlView-1 satellite imagery, symbol size is classified planimetric coastal erosion rate, color coded symbology displays volumetric erosion from 1951 until 2010 for 118 coastline segments; right: difference raster from multitemporal DEMs representing elevation changes over 59 yr.

TCD
7, 4101–4176, 2013

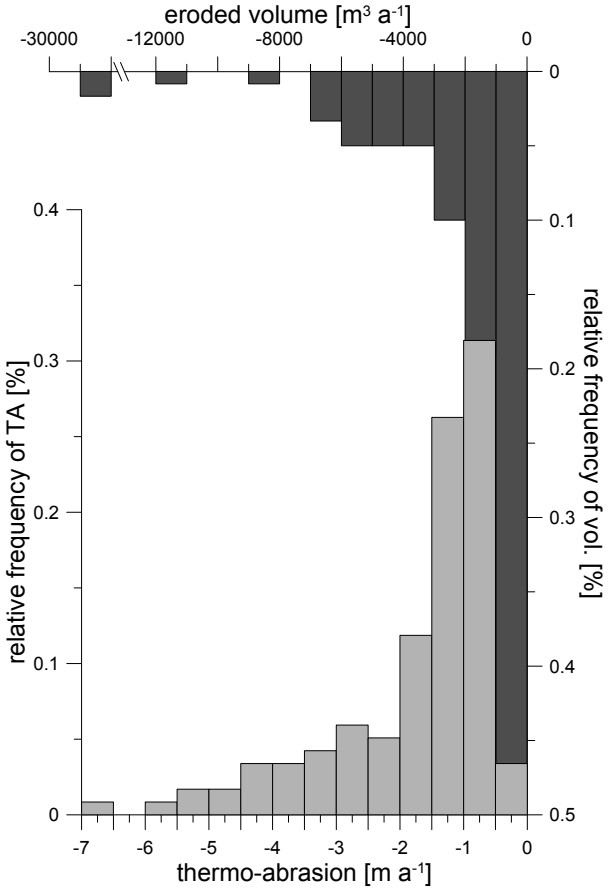

Fig. 12. Histograms of thermo-abrasion during the historical period from 1951 to 2010 and associated volumetric land loss on Muostakh Island.

TCD
7, 4101–4176, 2013

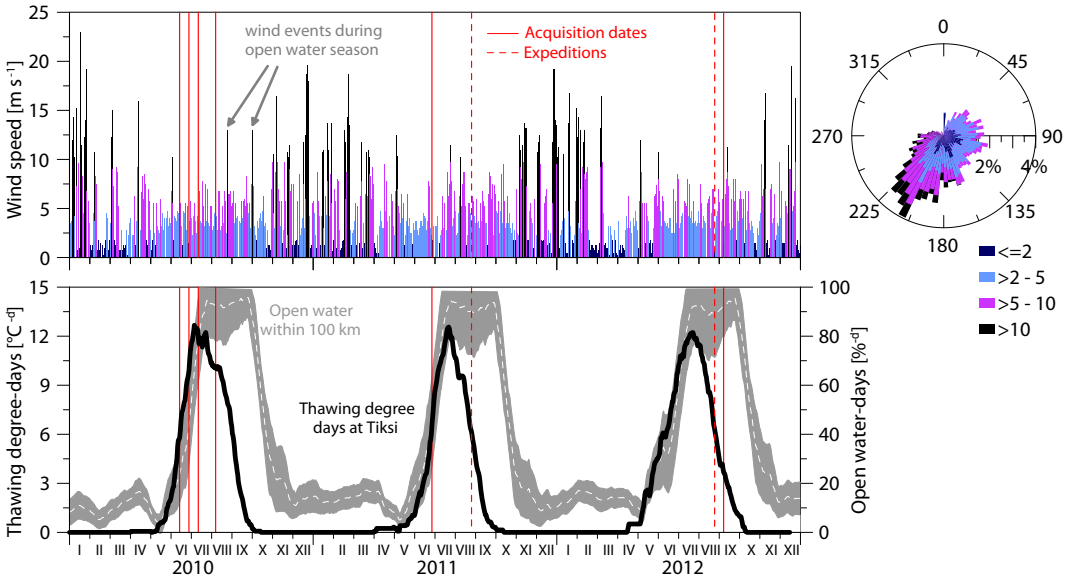

Fig. 13. Seasonal fluctuations of degree days thawing (DDT) and open water days (OWD) within a 100 km radius around Muostakh Island. Bars of wind speeds measured in the nearby town of Tiksi, all for the period 2010–2012. Straight through lines mark satellite image acquisitions, dashed lines topographic surveys during on-site visits, all with uneven distribution. Note the seasonal shift of summer air temperatures and open water period.

TCD
7, 4101–4176, 2013

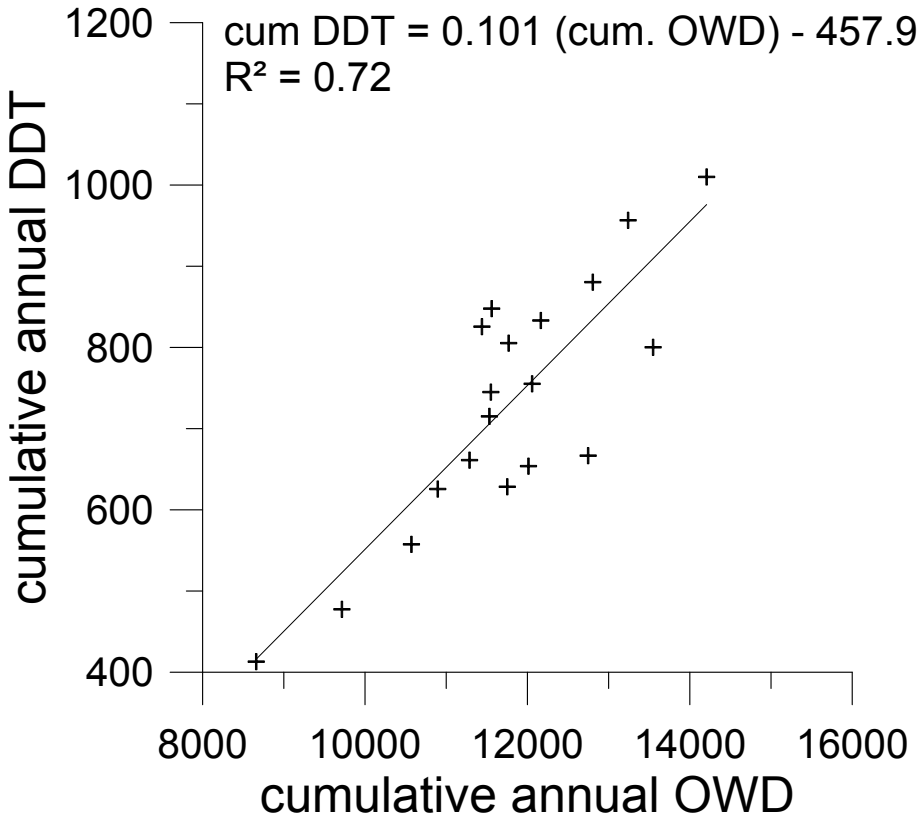

Fig. 14. Cumulative DDT and OWD for the overlapping reference period of both records (1992–2012) shows dependancy in relation of DDT and OWD.

TCD
7, 4101–4176, 2013

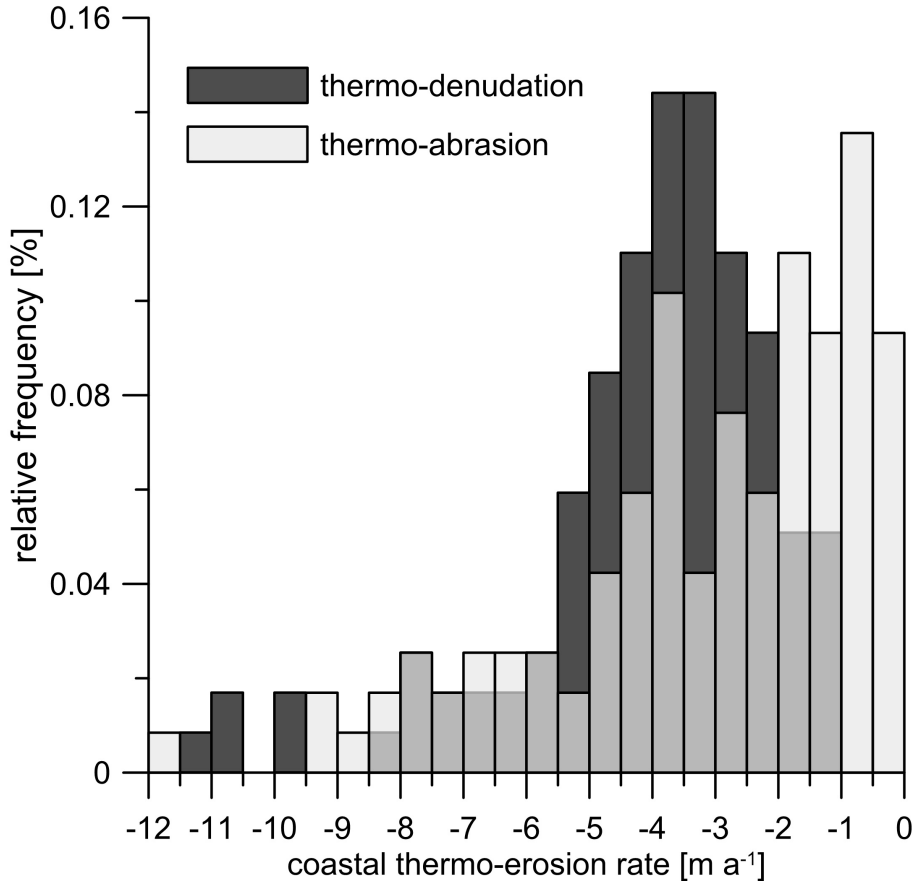

Fig. 15. Histograms of mean annualized coastal erosion rates m a^{-1} on Muostakh Island, obtained from segmentated coastlines. Thermo-denudation rates were corrected using a DDT season factor and thermo-abrasion rates considering actual length of the sea ice free season.

TCD
7, 4101–4176, 2013

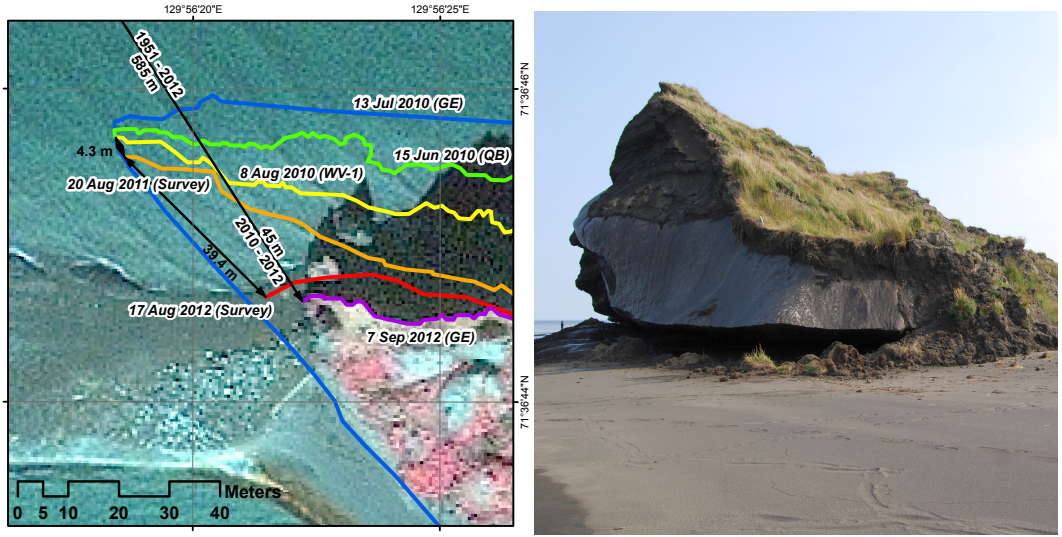

Fig. 16. Close up view of coastal erosion at the northern cape of Muostakh Island. Left: selected cliff top position lines of the 2010–2012 period. Blue line outlines cliff bottom position in early 2010. Ends of cliff top lines are at sea level, marking the northernmost point of the island. Right: photograph of the northern cape (8 August 2012).

TCD
7, 4101–4176, 2013

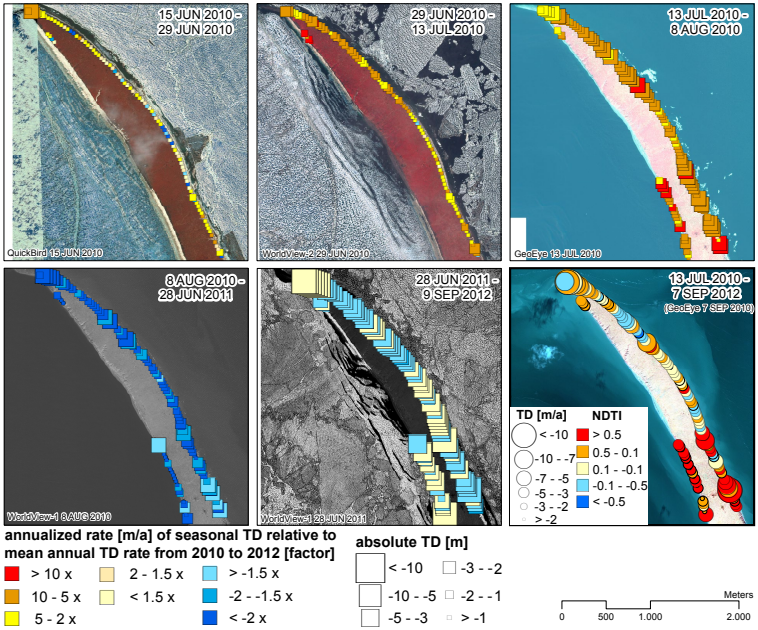

Fig. 17. Thermo-denudation (TD) during current periods of observation using very high resolution remote sensing data. Symbol size is equivalent to retreat in m (periods 1–5), color coding expresses matching of TD rate calculation to mean TD rates over the 2010–2012 period, shown in lower right. Differences of < 5 × arise from varying intensities between seasons, while differences of > 5 × reflect TD overestimations through annual change rate calculation, based only on seasonal observations. Upper left: period 1 (spring 2010); upper middle: period 2 (summer 2010); upper right: period 3 (summer); lower left: period 4 (fall 2010, partially spring 2011); lower middle: period 5 (2011–2012); lower right: 2010–2012 interannual observation period, symbol size equivalent to TD [ma^{-1}], color coded Normalized Difference Thermo-erosion Index (NDTI) illustrates prevailing thermo-denudation (> 0.1) or -abrasion (< 0.1).

TCD
7, 4101–4176, 2013

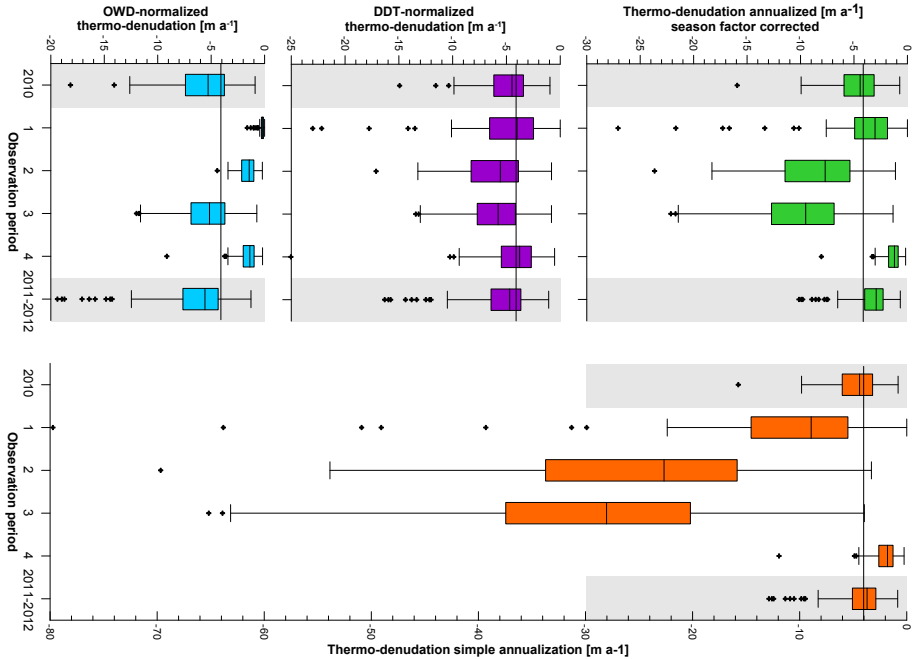

Fig. 18. Thermo-denudation (TD) rates for 6 different time periods (2010, 1 (spring 2010), 2 (summer 2010), 3 (summer 2010), 4 (fall 2010), and 2011–2012) are shown as box plots that include data from all 118 coastline segments. Correction procedure counterclockwise, mean TD for 2010–2012 as reference line. Right series (orange): measured TD normalized to the observation period (corresponds to the rates normally reported in the literature); lower left (blue): TD rates normalized using open-water days (OWD); middle left (purple): similar normalization using the cumulative degree days thawing (DDT) for each period, which produces roughly comparable rates; upper left (green): shows the normalization to the length of the DDT season during the observation period.

TCD
7, 4101–4176, 2013

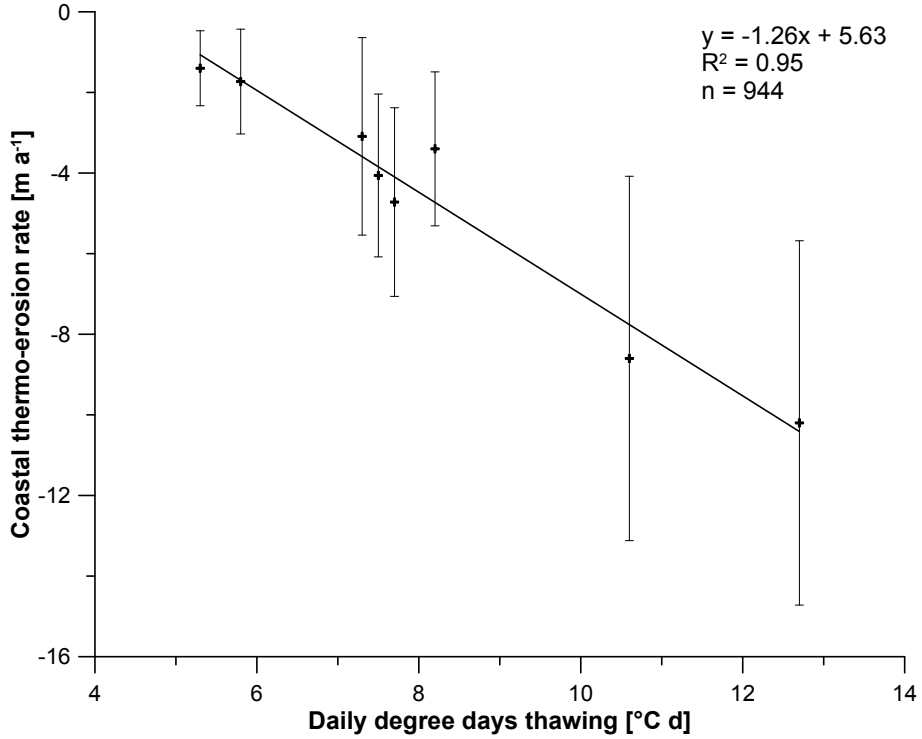

Fig. 19. Mean annual coastal thermo-erosion (6 data points for TD and 2 for TA) vs. mean daily positive air temperature. Each erosion data point is a mean of all 118 coastal sections, error bars are built of standard deviation of rates. Mean daily positive air temperature was calculated from cumulative degree days thawing (DDT) divided by the number of days with DDT occurance.

TCD
7, 4101–4176, 2013

Fig. 20. Photograph of catastrophic collapse through undercutting, reflecting activation of TA during rising water level at the end of August 2011, when sea water comes in contact with permafrost in the level of thermo-niches. Under calm weather conditions the ground ice block decayed within two days.

TCD
7, 4101–4176, 2013